Unravelling textural heterogeneity in obsidian: shear-induced outgassing in the Rocche Rosse flow

J.K. Shields[a,*], H.M. Mader[a], L. Caricchi[b], H. Tuffen[c], S. Mueller[d], M. Pistone[e], L. Baumgartner.[f]

[a]*School of Earth Science, University of Bristol, Bristol, UK.*
[b]*Section of Earth and Environmental Sciences, University of Geneva, Geneva, Switzerland.*
[c]*Lancaster Environment Centre, Lancaster University, Lancaster, UK.*
[d]*Institute of Geosciences, Johannes Gutenberg University Mainz, Germany.*
[e]*Division of Petrology and Volcanology, Smithsonian Institute, Washington, USA.*
[f]*Institute of Earth Sciences, University of Lausanne, Lausanne, Switzerland.*

Abstract

Obsidian flow emplacement is a complex and understudied aspect of silicic volcanism. Of particular importance is the question of how highly viscous magma can lose sufficient gas in order to erupt effusively as a lava flow. Using an array of methods we study the extreme textural heterogeneity of the Rocche Rosse obsidian flow in Lipari, a 2 km long, 100 m thick, $\sim$ 800 year old lava flow, with respect to outgassing and emplacement mechanisms. 2D and 3D vesicle analyses and density measurements are used to classify the lava into four textural types: 'glassy' obsidian ($<$ 15% vesicles), 'pumiceous' lava ($>$ 40% vesicles), high aspect ratio, 'shear banded' lava (20-40% vesicles) and low aspect ratio, 'frothy' obsidian with 30-60% vesicles. Textural heterogeneity is observed on all scales (m to μm) and occurs as the result of strongly localised strain. Magnetic fabric, described by oblate and prolate susceptibility ellipsoids, records high and variable degrees of shearing throughout the flow. Total water contents are derived using both thermogravimetry and infrared spectroscopy to quantify primary (magmatic) and secondary (meteoric) water. Glass water contents are between 0.08 - 0.25 wt.%. Water analysis also reveals an increase in water content from glassy obsidian bands towards 'frothy' bands of 0.06 - 0.08 wt.%, reflecting preferential vesiculation of higher water bands and an extreme sensitivity of obsidian degassing to water content. We present an outgassing model that reconciles textural, volatile and magnetic data to indicate that obsidian is generated from multiple shear-induced outgassing cycles, whereby vesicular magma outgasses and densifies through bubble collapse and fracture healing to form obsidian, which then re-vesiculates to produce 'dry' vesicular magma. Repetition of this cycle throughout magma ascent results in the low water contents of the Rocche Rosse lavas and the final stage in the degassing cycle determines final lava porosity. Heterogeneities in lava rheology (vesicularity, water content, microlite content, viscosity) play a vital role in the structural evolution of an obsidian flow and overprint flow-scale morphology. Post-emplacement hydration also depends heavily on local strain, whereby connectivity of vesicles as a result of shear deformation governs sample rehydration by meteoric water, a process previously correlated to lava vesicularity alone.

*Corresponding author
Email address: jessie.shields@bristol.ac.uk (J.K. Shields)

Keywords: obsidian, outgassing, emplacement, Rocche Rosse, heterogeneity

1. Introduction

1.1. Effusive silicic volcanism

The generation and emplacement of effusive silicic lava provides an ongoing conundrum for volcanologists. Magma viscosities on the order of 10^8 to 10^{12} Pas [e.g. 1] inhibit bubble growth and contribute to volatile oversaturation in the melt as rhyolitic magma ascends to lower pressures and depths in the conduit [e.g. 2]. Solubility calculations show that if magma contained dissolved water in concentrations typical of obsidian lava (0.1-0.4 wt.%) decompression during ascent would result in vesicularities far beyond those inferred for fragmentation [3]. Therefore to avoid explosive fragmentation of ascending magma there must be significant volatile removal from the melt i.e. open-system degassing (outgassing) in order to reduce gas overpressure [e.g. 4, 5, 6] and result in effusion of degassed obsidian lava.

Previous authors have recognised that gas escape through permeability development in the conduit is vital for the generation of obsidian, and several mechanisms have been proposed. Early work by [5] suggested that silicic magma rises as a highly permeable foam which, upon extrusion, loses gas via development of bubble connectivity, enabling outgassing to the conduit walls [7]. Another body of work describes shear-induced fracturing of magma, leading to permeable pathways through which volatiles can escape [8, 6, 9, 10, 11]. There is widespread evidence for this non-explosive magma fragmentation, in the form of brittle fracture and healing. Observations of transient pyroclastic channels, or tuffisites, have been made at numerous volcanoes: Mule Creek Vent, USA [8], Torfajökull, Iceland [12], Chaitén, Chile [11] as well as explosive products from the Monte Pilato-Rocche Rosse eruption, Lipari [13]. These veins of welded fragmental material describe shear fracture and healing of silicic magma [12] and may result in dense bubble-free obsidian bands [14, 15, 16, 13].

[17] experimentally show the effect of shear on outgassing of viscous magmas, highlighting significant localisation of shear strain during deformation. Some authors postulate that localised shear-induced fracture alone is not an effective large-scale outgassing mechanism and that a combination of permeability via bubble connectivity and fracture development is required to fully outgas ascending magma [11, 18, 19] and result in volatile-poor obsidian lava. Most recently [20] suggest a combined explosive-effusive eruption style is responsible for obsidian generation, where tuffisite veins act as long-reaching pathways for gas removal from closed-system magma batches, resulting in lava effusion accompanied by pyroclastic fountaining and explosions [21, 22].

Extreme textural heterogeneity of obsidian lava suggests that outgassing is a complex process and may continue during surface flow. When erupted, obsidian lava flows display a range of magmatic water contents, vesicularities and structural features that raise questions about mechanisms of obsidian emplacement and post-emplacement processes. [5], as part of the permeable foam model, suggests that dense obsidian is formed from collapse of foamy magma upon extrusion, and that any heterogeneities in vesicularity are the result of incomplete bubble collapse. This idea was refuted by [23], who also recognised evidence for sec-

ondary exsolution of volatiles during surface flow. They suggest that a degree of volatile stratification exists in the conduit that contributes to the different water contents observed in eruptive products. [24] and [25] suggest a layered structural model for obsidian flows, composed of glassy obsidian, crystalline rhyolite, pumiceous and brecciated zones. We build on this model by investigating textures and volatile contents in the surface of an obsidian flow.

A particular difficulty when analysing lava flows is determining the degree of strain undergone by the rock, a parameter shown to be fundamental for studies of lava outgassing. Strain is notoriously difficult to extract from natural lava samples. Strain markers, such as microlites, magmatic enclaves and deformed bubbles have been used [26, 27, 28], however these techniques can be complex, time consuming and require extensive sample preparation. In this study we use a simple, precise and extremely rapid technique which requires minimal sample preparation: measurement of the Anisotropy of Magnetic Susceptibility *AMS*, to determine the shapes and degree of anisotropy of the ellipsoid of magnetic susceptibility in various samples [e.g. 29]. This, in combination with a detailed petrographic study and 2D and 3D characterisation of the samples, reveals the relationships between AMS and the distribution of strain within the obsidian flow. Furthermore, we overcome issues surrounding the interpretation of deformed bubble textures in thin sections (stereology) by using 3D computed tomography analysis. We also analyse obsidian density, vesicularity, hydration by meteoric water and magmatic water contents.

By combining an array of methodologies we determine the importance of strain localisation on the outgassing and emplacement of obsidian. The focus of this study is the Rocche Rosse lava flow, Lipari. With this field example we quantify the distribution of obsidian flow physical properties and propose a gas loss model that can account for the textural heterogeneity observed in effusive silicic eruptions.

1.2. Rocche Rosse flow description

The Rocche Rosse (*RR*) lava flow in Lipari, Aeolian Islands (Figure 1), represents the final, effusive stage of the most recent eruptive activity from the Monte Pilato pumice cone on Lipari Island, which ended in 1220 ± 30 AD [31] and produced a 2 km long, 100 m thick, almost aphyric rhyolitic pumice and obsidian flow [32]. Approximately 400 years prior to lava effusion the Monte Pilato cone erupted explosively, producing over 200 m thick pumice deposits [33]. Whole rock chemistry is the same for explosive and effusive products [34, 13], except for a marked decrease in volatile content from maximum 0.9 wt.% H_2O measured in glassy rinds of obsidian pyroclasts to ~ 0.2 wt.% in obsidian lava [35, 32, 13].

The *RR* extends NNW from the vent and appears to be formed of two major 'lobes'; one to the west and one to the east (Figure 1, showing east lobe). The flow displays large and small scale folding, pervasive flow banding (sometimes enhanced by spherulite crystallisation) and a blocky, fractured upper surface, which often forms ramp structures. Only the uppermost several metres of the flow are accessible. Textures associated with flow emplacement are complex and reflect the large strains experienced during progressive lava extrusion. Glassy obsidian layers are found alongside more volatile-rich material. Compositionally the lava is calc-alkaline, and contains approximately 74 wt.% SiO_2, 5 wt.% K_2O and < 1 wt.%

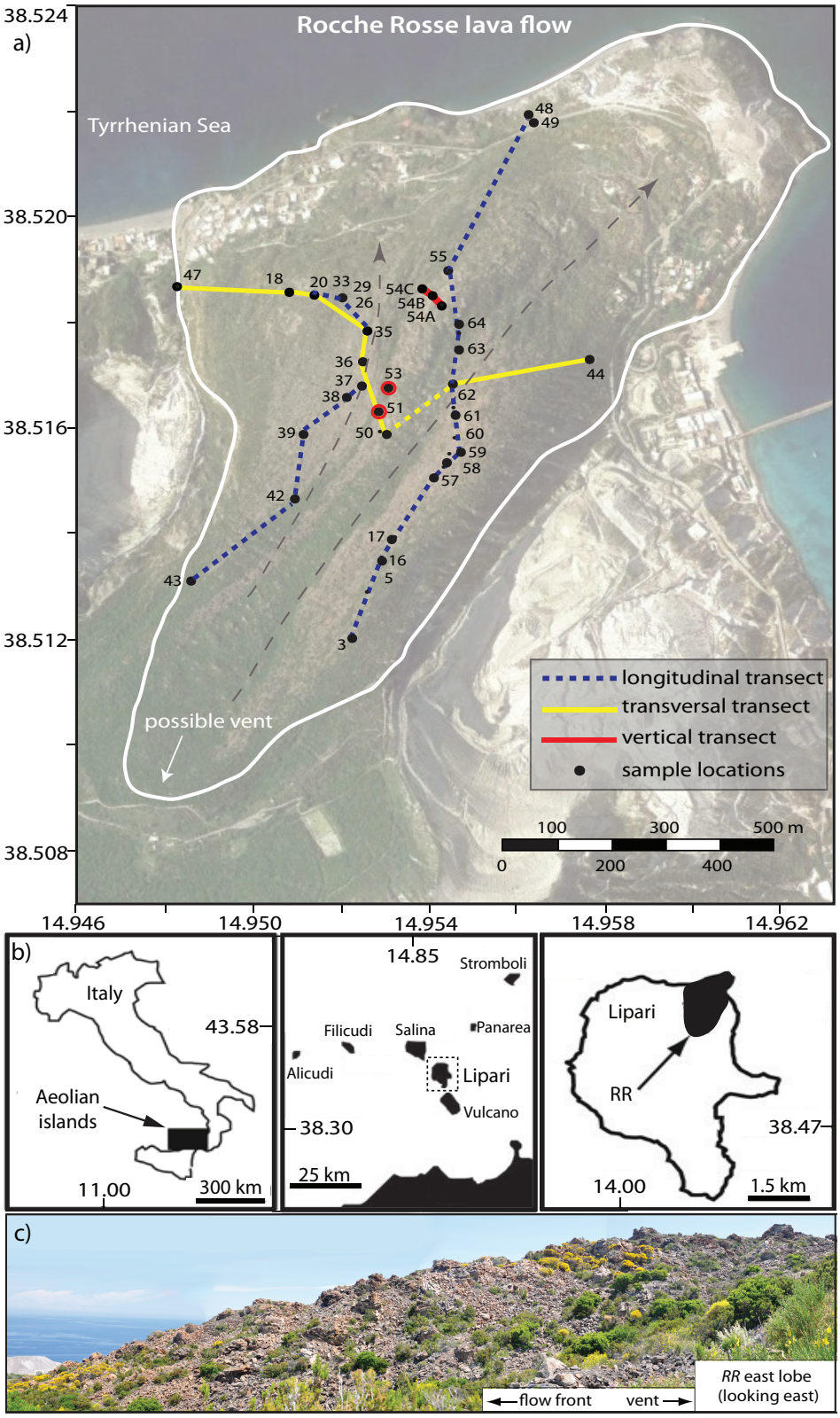

Figure 1: a) Map of the Rocche Rosse lava flow (source: Google Earth) showing sampling and transect locations. Numbers refer to sample names. Vertical transects (red lines) include multiple samples at each point. Axes are latitudinal and longitudinal coordinates. Flow outline taken from the geological map of Lipari island by [30]. b) Schematic map of location of Aeolian islands, Lipari and the RR flow, adapted from [13]. c) Photograph of east lobe of the RR lava flow (credit: L. Caricchi) showing clinkery surface texture and flow ramp features.

H_2O [33, 35, 32, 36]. A high alkali content and an eruptive temperature of > 850 °C [37, 38] have been used to explain the anomalous length of the *RR*, as these factors lower magma viscosity and increase mobility of obsidian flows [39, 40].

Previous work on the Rocche Rosse includes a petrological and geochemical study by [32] which interprets the *RR* as a superheated, initially water undersaturated magma that degassed in the upper conduit. It is thought that the lava is the result of fractional crystallisation of a latitic magma, with a degree of crustal assimilation [41, 32, 39]. These authors infer that an injection of a more mafic melt was the trigger for the explosive phase of the eruption [39]. [32] see no noticeable variation in magmatic water content between pumice and obsidian samples and infer that the obsidian could be formed as a result of pumice collapse during flow.

Several studies exist on the devitrification textures found in the *RR*, which occur throughout in the form of spherulites, axiolites and lithophysae [42, 43, 44]. Growth of these anhydrous crystalline aggregates, comprising alkali feldspars and cristobalite [45, 46] is controlled by H_2O diffusion through the melt and can occur throughout cooling, both above and below the glass transition interval (620 - 750 °C) [45, 44, 47].

[35] use relaxation geospeedometry to model cooling rates of 0.2 - 0.3 °C/min and a glass transition temperature of 676 - 706 °C for the *RR* flow fronts, and postulate that the lava would be actively deforming during flow for days to weeks after the eruption had ceased at the vent, consistent with subsequent observations of obsidian flow advance at Cordón Caulle [22]. [44] suggests this would be important for spherulite growth and deformation as nucleation would have started in response to large undercoolings at temperatures above the glass transition (> 800 °C) then continued with hydration at lower temperatures (< 300 °C) on timescales of up to 400 years, with some spherulites forming prior to foliation textures and others nucleating long after flow ceased.

To date no study of the degassing and emplacement processes of the *RR* and no quantitative analysis of the extreme heterogeneity in flow physical properties has been carried out. As well as unravelling the complexities of obsidian degassing and emplacement processes, we map, identify and interpret patterns in the distribution of strain and outgassing in the *RR* flow and offer new insights on the generation of obsidian lava. For clarity 'degassing' and 'outgassing' are defined explicitly here as 'the loss of volatiles from the melt phase (exsolution)' and 'the removal of dissolved or exsolved volatiles from the magma', respectively, following [48].

2. Methods

2.1. Macroscopic and microscopic textural description

Observations were made at 60 locations along various transects across the lava flow (Figure 1). Lava samples were collected at each location and brought back for analysis. The sampling procedure was designed to cover the spatial extent of the lava flow as best as possible whilst ensuring outcrops were intact and free of vegetation. Samples of *RR* lava repre-

senting the range in observed textures (locations shown in Figure 1) were described in hand specimen, by optical microscopy of polished thin sections and by 3D X-ray tomographic CT scans. Thin sections were oriented in a plane perpendicular to the shear plane which contains the shear direction (Figure 2a). Typically the shear direction is parallel to the flow direction, marked by aligned vesicles (i.e. 'fossil' bubbles, as opposed to gas-pressurised pockets in the melt) and flow banding. This plane is the most suitable for analysing shear induced fabric development.

2.2. Density and bulk vesicularity

Prior to density determination, rock specimens (10 - 100g) were dried at > 100 °C for 24 hours to remove atmospheric water. Samples were then individually sealed using impermeable plastic paraffin film and first weighed in air M_{air} then submerged in water M_{water} using a Mettler Toledo XS204 balance and density measurement kit, with an uncertainty in mass measurement of ± 0.001g. Bulk density ρ_{bulk} and volume V of samples were derived using Archimedes principle. Vesicularity ϕ_{dens} (%) was calculated using:

$$\phi_{dens} = \frac{\rho_{DRE} - \rho_{bulk}}{\rho_{DRE}} x100 \quad (1)$$

where ρ_{DRE} is the dense rock equivalent density of the magma (2.189 g/cm^3), calculated at room temperature using the calculation method of [49], data from [50] and the major element composition of Lipari obsidian from [35].

2.3. 3D vesicle textures

2.3.1. X-ray tomography

Cylindrical cores of 8 selected samples, top parallel to the shear plane, approximately 25 mm long and 25 mm diameter (Figure 2b), were scanned using X-ray tomography (University of Lausanne). Samples were selected to represent the different textures observed in hand specimen. Sample size was chosen to attempt to capture both macroscopic-scale features as well as microscopic vesicles. A high-resolution μCT scanner (Skyscan® 1173) was operated at 110 kV and 80 μA and a 1 mm Al-filter. Shadow projections with an image pixel size of 14.96 µm and an average of 30 frames (exposure time: 700 ms) were taken for each rotational step (360° rotation in steps of 0.2°).

The differences in X-ray attenuation between glass and vesicles are represented as different grey-scale values, allowing for distinction of the two phases. Skyscan® NRecon software was used for reconstruction of the shadow projections to obtain a stack of horizontal CT slices (Figure 2b). A standardized post-processing procedure (post-alignment, beam-hardening, ring-artifacts and smoothing) was performed at this step to provide the best image quality. CT images are then cropped using CTAn software (Skyscan® v.1.12) to omit the outer edge of the sample to minimise edge effects.

2.3.2. 3D analysis

Volumetric and geometric measurements of vesicles were performed on the CT images using Blob 3D software [51]. Vesicles were segmented from the glass matrix by defining a greyscale threshold range for each sample, using an identical method to that described in

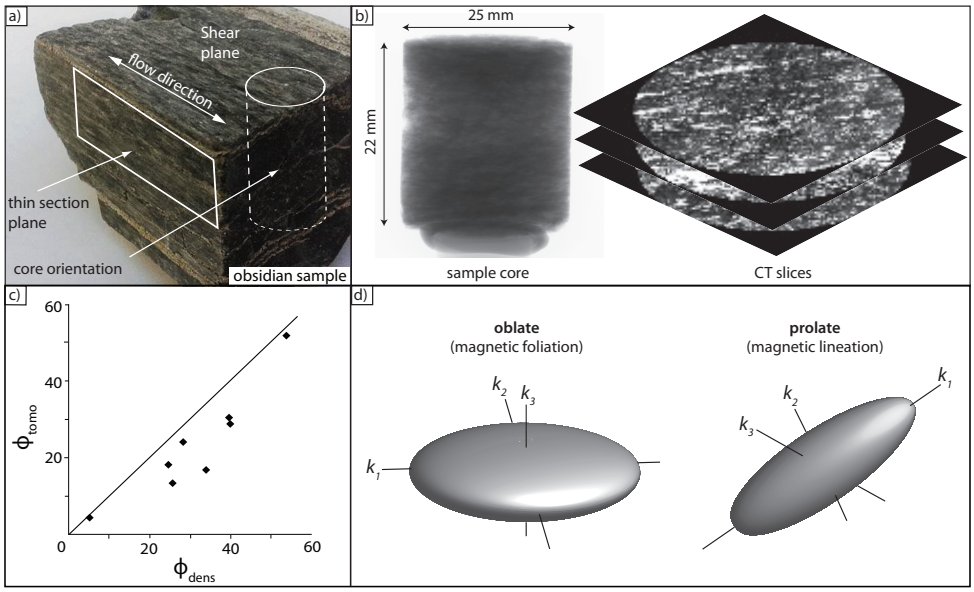

Figure 2: a) Photograph of an obsidian sample showing the thin section plane, tomography core orientation, the shear plane and the flow direction inferred from vesicle lineations. b) X-ray tomographic image of sample core 54C1 and a stack of 3 CT slices of the same sample. (Actual number of slices in a sample is 1902.) c) Comparison of vesicularities of RR samples determined from 3D tomography and density measurements. d) Sketch of oblate and prolate AMS ellipsoids with principal axes orientations. k_1 = maximum axis, k_2 = intermediate axis and k_3 = minimum axis.

[17]. Image resolution was downsampled by a factor of 2 to enable processing with Blob3D. Spatial resolution of CT images after processing was 29.92 μm per pixel therefore 3D voxels each contain 2.68x10^4 μm^3. The smallest vesicles are not well defined at this resolution therefore 6 voxels was taken as the minimum object size, resulting in a minimum object diameter (assuming a spherical shape) of 68 μm.

Data extracted includes vesicularity ϕ_{tomo}, vesicle size, and aspect ratio *AR*. Vesicularity calculated from CT images agrees well with that determined from density measurements (Figure 2c), although tomography values consistently underestimate vesicularity by approximately 25 % as a result of scan resolution and the omission of vesicles $<$ 68 μm diameter. As a result of the low spatial resolution CT images further analyses were carried out in an attempt to improve quantitative interpretations of strain (section 2.4) and vesicle connectivity (section 2.5) in *RR* samples.

2.4. Magnetic properties

Measurement of the anisotropy of magnetic susceptibility (AMS) of rocks is a fast and precise technique used to quantitatively describe the magnetic fabric of rocks based on alignments of magnetic minerals. In contrast to x-ray tomography AMS analysis can be performed in minutes, with very high precision, and does not require high computational capabilities. By combining AMS results with a thorough analysis of rock textures one can obtain information on lava flow dynamics, and specifically quantify shear strain [52, 53, 54, 55]. Many studies identify correlations between the shape of the magnetic susceptibility ellipsoid and the shape of the strain ellipsoid [56, 57, 58, 53, 59, 60, 61], however they are not necessarily equal [56, 58]. Magnetic anisotropy is affected by magnetic grain shape and distribution as

well as the deformation mechanism [e.g. 62, 63]. Therefore in order to interpret the magnetic fabric of a rock in terms of its strain history it is vital to determine the identity and properties of the magnetic minerals contributing to the magnetic susceptibility [55].

Bulk magnetic susceptibility per unit volume of rock K is the ratio of the intensity of magnetisation, M (A/m), to the the intensity of the applied magnetic field, H (A/m). Therefore K is dimensionless and varies with the strength of the applied field. Magnetic anisotropy is reflected by a variation in M with sample orientation within the magnetic field. AMS measurements were performed on cylindrical lava samples 25 mm diameter, 22 mm length (constant volume) using a spinning MFK-1 FA Kappabridge instrument at the University of Geneva, Switzerland. Measurements of low field (300 A/m) susceptibilities were taken at room temperature using an operating frequency of 976 Hz. During sample rotation on each of the 3 axes 64 measurements were taken over 360 °. Sensitivity of the instrument is 2×10^{-8} and measurement accuracy is $\pm$ 0.1 %. The samples were not oriented in the field but the top of the cylinder was always chosen as parallel to the inferred shear plane.

Characteristic variations in K with temperature can be used to identify the magnetic minerals which contribute to the measured magnetic susceptibility [58, 60, 64]. Three selected samples were heated in Argon up to 700 °C and cooled back to room temperature whilst continually measuring the magnetic susceptibility. A rapid change in susceptibility is interpreted as the Curie temperature (supplementary material). Thin sections were carefully analysed to determine grain size, shape, distribution as well as amount of magnetic minerals (% of total area) in each sample.

Variation in K is described by a susceptibility ellipsoid (Figure 2d), defined by the maximum, intermediate and minimum principal susceptibility tensors (k_1, k_2, k_3 respectively), which form the three orthogonal axes of the ellipsoid. The geometric mean susceptibility of each sample K_m is used to numerically describe K. Anisotropy of sample magnetic susceptibility is given by the corrected degree of anisotropy P_j, which increases proportionally to the anisotropy of the ellipsoid. If magnetic fabrics are generated by deformation, the P_j parameter is a direct measurement of the *amount of applied shear strain*. In this case the shape of the susceptibility ellipsoid is analogous to the *shape of the strain ellipsoid* [65], described by the shape indicator T (Figure 2d). $T > 0$ describes an oblate magnetic susceptibility ellipsoid (Figure 2d), which indicates a magnetic foliation [e.g. 66]. $T < 0$ describes a prolate magnetic susceptibility ellipsoid, which indicates a magnetic lineation. In oblate samples k_3 represents the axis perpendicular to the magnetic foliation plane.

2.5. Vesicle connectivity

Connected vesicularity was determined for *RR* samples of known volume using a helium pycnometer. The volume of solid phases plus the volume of any non-connected vesicles was measured V_{meas}, and connected vesicularity was then given by 1 - (V_{meas}/sample volume), after [67]. Connected vesicularity is related to sample permeability, however the tortuosity of connected pathways, not measured here, also affects the permeability of magma [68].

2.6. Volatile content measurements

Samples of quenched obsidian effectively preserve non-exsolved volatiles within the silicate glass structure [69], thereby enabling the study of degassing processes through quantification of volatile concentration. Magmatic glasses typically contain both primary (magmatic) and secondary (meteoric) water [70, 71, 72], the latter recording hydration by external water, which diffused into the glass post eruption, plus water adsorbed during sample preparation [73].

It has been assumed previously that, at the low water concentrations characteristic of obsidian (< 1 wt.%), water dissolves in the glass predominantly as hydroxyl groups OH^-, as a result of equilibrium speciation [74, 75]. However, speciation is dependent on cooling rate, and when lava cools slowly equilibrium speciation cannot be maintained and both OH^- and molecular water H_2O_m will contribute to total water content [76, 77, 78, 79]. Molecular water may also be added during low temperature hydration e.g. during resorption of exsolved water on cooling [80] or the diffusive ingress of meteoric water [46].

2.6.1. Thermal Gravimetric Analysis (TGA)

Multi-species volatile contents and degassing patterns of 16 obsidian samples (representing a wide spatial distribution) were characterized by simultaneous differential scanning calorimetry-thermogravimetric analysis (DCS-TGA) using TA Instruments SDT Q600 and STA 449 devices, following the methods set out in [81] and [82]. The DSC-TGA technique subjects the sample to a controlled heating programme (0 - 1250 °C at 5 °C/min), during which sample weight and differential heat flow are continually measured. From the weight loss curve (TGA curve) we calculate the total volatile content TVC (wt.%) of the sample. Furthermore, the derivative of the TGA curve (dTG curve, shown in supplementary material) gives the rate of weight loss with time, from which we measure the peak degassing temperature, which gives information on the speciation of volatiles [72, 83]. dTG peaks depend on many factors, including grainsize, heating rate, spatial distribution of water within grains, and volatile concentration [83, 73].

An inert, volatile-free, high purity Al_2O_3 powder standard was used to check for change in the TGA curve over time and to produce a reference TGA curve that was then subtracted from sample TGA curves to account for instrument drift at low mass loss and yield actual sample weight loss (supplementary material). Approximate errors due to reproducibility of the weight baseline are $\pm$ 0.05 wt.%.

2.6.2. Fourier Transform Infrared spectroscopy (FTIR)

Whilst the TGA method can reveal some volatile speciation it cannot fully discriminate between water, carbon dioxide and halogen contents. FTIR allows quantification of both molecular water (H_2O_m) and hydroxyl groups (OH^-), as well as carbon dioxide (CO_2) in silicate magmas [84]. Total water dissolved in the silicate glass H_2O_t was measured via the 3550 cm^{-1} absorbance peak. The 1630 cm^{-1} absorbance peak was measured to check the contribution from molecular water H_2O_m.

Doubly polished wafers 100 - 200 μm thick were prepared and minimum 6 transmission

spectra for each sample were obtained on spot sizes of 100 μm - 200 μm with a Nicolet iZ10 FTIR Spectrometer, using a CaF_2 Beam Splitter, KBr disk, Hg source, MCT/A detector and a spatial resolution of 4 cm^{-1}, in the range 6500 cm^{-1} to 500 cm^{-1}. Absorbance peak heights (intensities) were corrected by subtracting a background spectrum after every sample and converted to H_2O molar concentration using the Beer-Lambert Law. Molar absorption coefficients, calibrated using glasses of known water content, are taken from [85] and [70] respectively i.e. ε = 75 $\pm$ 4 l/mol/cm (3550 cm^{-1} peak) and 55 $\pm$ 2 l/mol/cm (1630 cm^{-1} peak).

3. Results

3.1. Rocche Rosse lava classification

Samples of *RR* surface lavas display highly heterogeneous textural characteristics. We group these characteristics into four distinct textural lava types, similar to those identified stratigraphically by [24]. Classification is based primarily on vesicularity ϕ_{dens} as well as 3D vesicle size (d_{mode} = modal vesicle diameter, d_{mean} = mean vesicle diameter, both in μm), shape (AR = vesicle aspect ratio) and connected vesicularity (Figures 3 to 7). Banding, spherulite content and TVC are also used to further describe lava types and are detailed in Table 1. Whilst textural analysis reveals abundant microscopic shear localisation features showing heterogeneity on μm scales (Figures 3 to 6), the dominant lava characteristic of the hand specimen (cm-m scale) is used to classify the samples. One sample (47) is omitted from the classification table due to it being completely re-welded breccia (Figure 8), located at the base of the flow on the west side (Figure 1). Principal characteristics of each category are summarised below.

3.1.1. Type 1: glassy obsidian

Type 1 is glassy and typically black in appearance (Figure 3a). It is poorly vesicular (ϕ_{dens} $<$ 15 %), high density ($\rho_{bulk} > 2.0\ g/cm^3$) and can be very spherulitic ($<$ 60 % by area). Vesicles are small (d_{mode} = 100 μm i.e. radius = log 1.7 μm, and d_{mean} = 124 μm, Figure 3d) and highly elongated parallel to the inferred shear plane ($\overline{AR}$ = 8.5, Figure 3b and e). Mean connected vesicularity and P_j are low (0.12 and $<$ 11 % respectively, Figure 7). Penetrative planar foliations i.e. flow banding are common in glassy obsidians (Figure 3c). Banding results from variable vesicularity, spherulites and/or microlite concentration or foliations of flattened vesicles/vesicle-free glass, which often define sinusoidal shear bands. Shear bands suggest strongly localised strain and, in hand sample, correlate to black glassy obsidian bands. Bubble collapse textures are common in type 1 samples, which include thick vesicle walls, few, small vesicles with homogeneous size distributions (Figure 3c and d). Glassy obsidian is found in both massive and platy (cm thick detached layers) outcrops (e.g. Figure 9a). Sample 35 was taken from the central portion of a 10 cm-wide shear zone that formed a vertical squeeze-out structure.

3.1.2. Type 2: 'frothy' obsidian

Type 2 is both vesicular (ϕ_{dens} = 30 - 60 %) and glassy in hand sample (Figure 4) with large (d_{mode} = 100-200 μm and d_{mean} = 207 μm, Figure 4i), sub-rounded vesicles elongated perpendicular to banding ($\overline{AR}$ = 2.5, Figure 3e, f, g and j). Mean connected vesicularity of

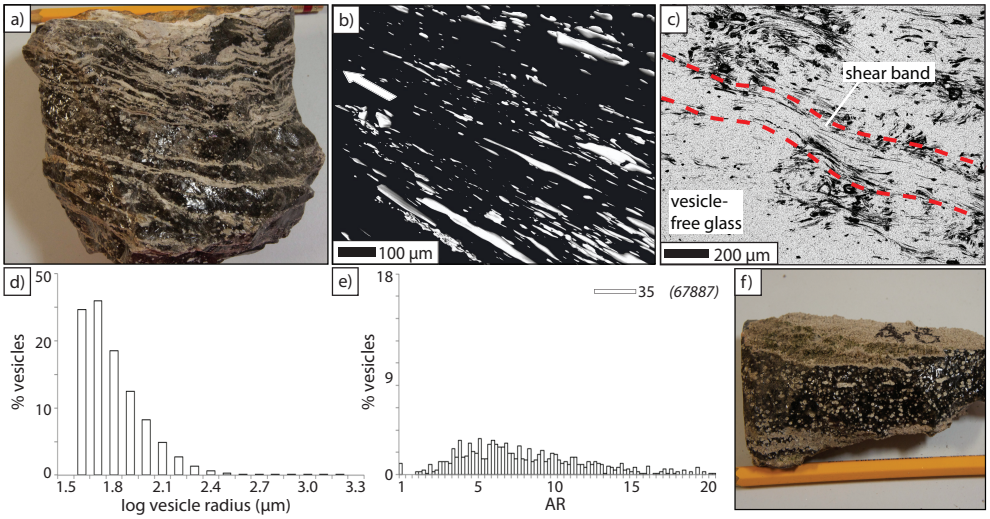

Figure 3: Representative images of glassy obsidian RR samples. a) Photograph of sample 3, showing black obsidian glass and spherulite trails. b) 3D rendered image of sample 35 showing highly flattened vesicles elongated parallel to shear (shown by arrow). c) Optical microscope image of sample 62 showing sinusoidal shear band of flattened vesicles. d) Vesicle size distribution VSD and e) aspect ratio AR histograms of type 1 sample 35 analysed in 3D. Vertical axis on both plots is number of vesicles as a percentage of total vesicles in the sample. Horizontal axis on VSD plot is the logarithm of the equivalent spherical vesicle radius. Italic figure in brackets show number of vesicles analysed per sample. Note horizontal axis on AR plot is twice as long as AR plots for other lava types. f) Photograph of sample 48, showing numerous isolated spherulites.

type 2 samples is 0.24 (Figure 7). Type 2 lava is ubiquitous throughout the flow yet has a unique field setting: lenses of vesicular, or 'frothy', material are primarily found in fold hinges (Figure 4b and c), which commonly coexist with tension gashes, micro-folding and extensional fractures (Figure 9b and i). 'Frothy' obsidian can occur on mm - m scales in the flow (e.g. Figure 4d). Banding is typically defined by variations in vesicularity or microlite content (Figure 4e, f and g) and can be deflected around earlier vesicles (Figure 4h) as well as around spherulites. Late growth vesicles may also overprint microlite bands e.g. Figure 4g. Textures therefore record multiple stages of deformation.

3.1.3. Type 3: pumiceous lava

Type 3 is highly vesicular (ϕ_{dens} = 40 - 60 %), low density (ρ_{bulk} = 1.0 - 1.3 g/cm^3) lava of variable vesicle size (Figure 5) and irregular, coalesced vesicles elongated parallel to the foliation plane (e.g. Figure 5f), unlike type 2 lava. It is referred to here as pumiceous. In finely vesicular type 3 lava (Figure 5a-c) d_{mode} = 100 µm and d_{mean} = 130 µm (Figure 5g) and $\overline{AR}$ = 2.3 (Figure 5h). In coarsely vesicular type 3 lava (Figure 5d-f) d_{mode} = 100 µm and d_{mean} = 170 µm (Figure 5g) and $\overline{AR}$ = 3.2 (Figure 3e). In contrast to type 2 lava, connected vesicularity and P_j are high, up to 0.49 and 35 % respectively (Figure 7). Bubble coalescence textures are ubiquitous in pumiceous lava (and type 4 samples) i.e. complex vesicle shapes, thin, partially or wholly retracted vesicle walls (Figure 5e and f), preservation of which shows bubble coalescence occurring until the flow cooled. Pumiceous lava is found throughout the flow and, in common with all categories, outcrops in close proximity (mm - m) to other lava types. Some samples contain several mms wide black obsidian bands within the pumiceous hand sample (Figure 5d).

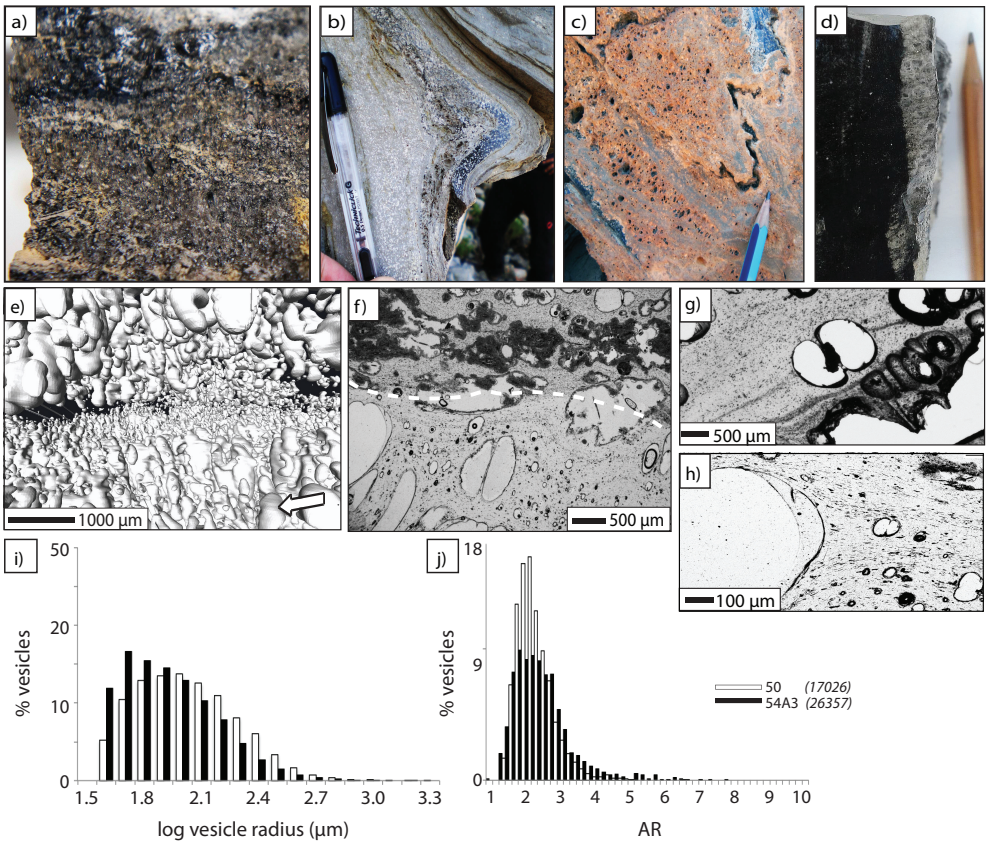

Figure 4: Representative images of 'frothy' obsidian RR samples. a) Photograph of type 2 lava (sample 50) in an ∼ 10 cm wide fold hinge (shown in c)) b) Localised 'frothy' lava in fold hinge of banded spherulitic obsidian. c) Micro-parasitic folds in vesicular and non-vesicular obsidian bands. d) Localised planar vesicle-rich lava in a glassy obsidian sample. e) 3D rendered image of sample 50 showing sub-spherical vesicles elongated perpendicular to shear with some coalescence parallel to shear. Sample also contains a glassy obsidian band parallel to shear shown by the absence of vesicles. Sense of local shear shown by arrows. f) Optical microscope image of sample 54A3 showing banded microlite-rich (top) and microlite-poor (bottom) layers as well as variable vesicle sizes. g) and h) Optical microscope images showing overprinting of microlite-defined flow fabric by vesicles in sample 51A1 and deflection of microlite-defined flow fabric by a vesicle in sample 54A3, respectively. i) Vesicle size distribution VSD and j) aspect ratio AR histograms of type 2 lavas analysed in 3D. Vertical axis on both plots is number of vesicles as a percentage of total vesicles in the sample. Horizontal axis on VSD plot is the logarithm of the equivalent spherical vesicle radius. Italic figures in brackets show number of vesicles analysed per sample.

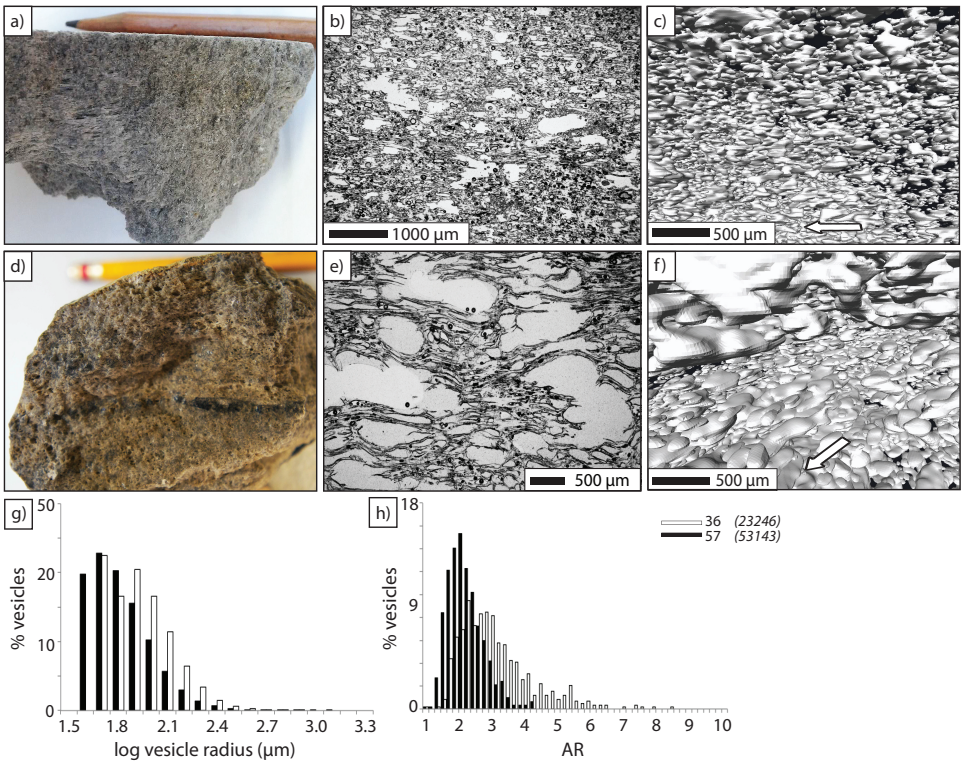

Figure 5: Representative images of pumiceous RR samples. a) Photograph of finely vesicular type 3 sample 16. b) Optical microscope image of sample 16 and c) 3D rendered image of sample 57 showing small, partly coalesced vesicles. d) Photograph of coarsely vesicular type 3 sample 36 with obsidian bands visible. b) Optical microscope image and c) 3D rendered image of sample 36 with larger coalesced and more elongate vesicles, as well as partially retracted vesicle walls and complex vesicle shapes (e)). Sense of local shear shown by arrows. g) Vesicle size distribution VSD and h) aspect ratio AR histograms of pumiceous lavas analysed in 3D. Vertical axis on both plots is number of vesicles as a percentage of total vesicles in the sample. Horizontal axis on VSD plot is the logarithm of the equivalent spherical vesicle radius. Italic figures in brackets show number of vesicles analysed per sample.

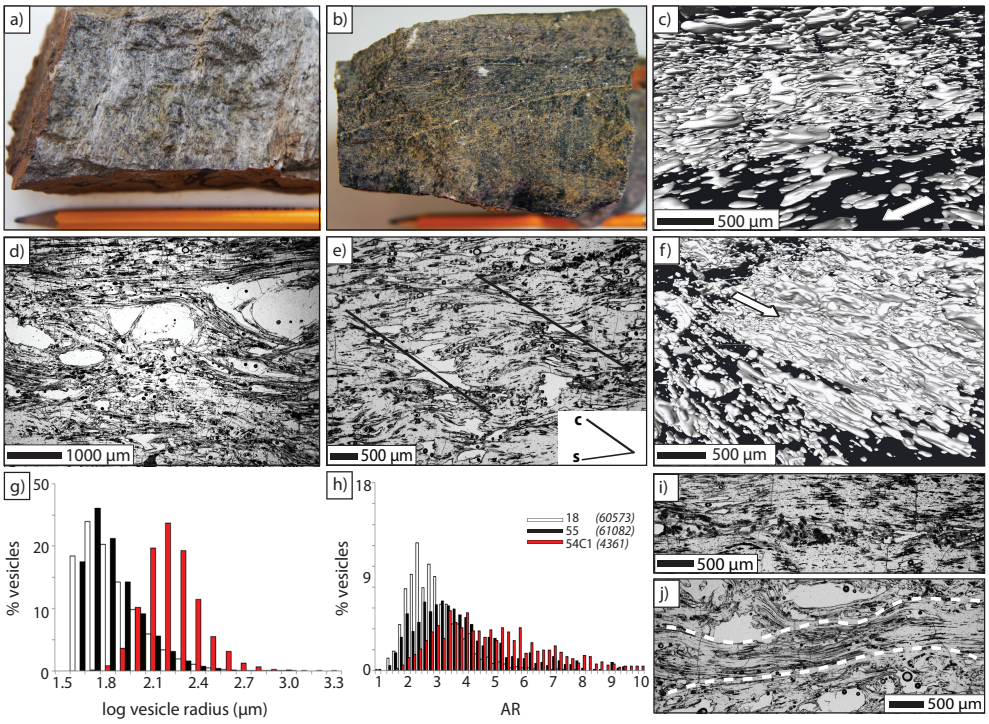

Figure 6: Representative images of shear banded RR samples. a) and b) Photographs of samples 54C1 and 54C2 showing sheared vesicle textures and obsidian bands. c) 3D rendered image of sample 55 illustrating high vesicle connectivity and irregular vesicle shapes. d) and e) Optical microscope images of samples 54C1 and 55, respectively, showing sigmoidal, high AR sheared vesicles, shear banding and S-C fabric in e). Inset shows orientation of S and C planes. f) 3D rendered image of sample 54C1 illustrating very high vesicle connectivity, elongation parallel to shear and localised differences in vesicle content. Arrows show sense of local shear. g) Vesicle size distribution VSD and h) aspect ratio AR histograms of type 4 lavas analysed in 3D. Vertical axis on both plots is number of vesicles as a percentage of total vesicles in the sample. Horizontal axis on VSD plot is the logarithm of the equivalent spherical vesicle radius. Italic figures in brackets show number of vesicles analysed per sample. i) and j) Optical microscope images showing a a plane of connected vesicular pore space parallel to shear in sample 54C1 and shear banding in sample 18, respectively.

3.1.4. Type 4: shear banded lava

Type 4 is a low-medium vesicularity lava (ϕ_{dens} = 20 - 40 %) with highly deformed and coalesced ($\overline{AR}$ = 2.7 - 5.0, Figure 6d, e, and h), irregular to flattened vesicles (d_{mode} = 100-316 µm and d_{mean} = 200 µm, Figure 6c, f and g). Connected vesicularity and P_j are again high, up to 0.38 and 48 % respectively (Figure 7). In some cases entire planes of connected vesicles are preserved (Figure 6i). In the field this sheared lava is often found in platy outcrops with cm-scale banding. Black diffuse obsidian bands are pervasive in type 4 samples (e.g. Figure 6b). Shear banded samples display clear strain fabrics, including brittle-ductile textures and frequent shear bands after which this lava type is named (Figure 6e and j). Typical S-C shear fabrics can be seen in type 4 samples (composing the foliation plane, S-plane, and the shear plane, C-plane, Figure 6e), which indicate degree of strain by the size of the angle between the two planes.

3.2. Nature and distribution of lava textures

Heterogeneous deformation is observed throughout the *RR* at multiple scales. Pervasive flow banding is a dominant macroscopic feature of the *RR*. Flow bands can be distinguished

Table 1: Rocche Rosse lava characteristics

Sample type	glassy obsidian					‘frothy’ obsidian				pumiceous lava			shear banded lava			
Sample	62	35	48/49	3	54B2	54A2	54A3	50	44C	57	16	36	18	54C1	55	54C2
ϕ_{dens} (%)	<1	5	10	6	5	40	34	40	34	40	40	54	26	28	25	18
d_{mode} (μm)	-	100	-	-	-	-	100	200	-	100	-	100	100	316	100	-
d_{mean} (μm)	-	124	-	-	-	-	180	234	-	130	-	170	134	336	130	-
Vesicle shape	flat	flat	n/a	flat	flat	reg- irreg	reg- irreg	reg- v irreg	reg- v irreg	reg- irreg	irreg	flat- irreg	flat- irreg	flat- v irreg	flat- irreg	flat- irreg
Modal *AR*	-	5.8	-	-	-	-	1.8	2.2	-	2.2	-	2.4	2.4	3.4	3.2	-
Vesicle elongation	∥ shear	∥ shear	∥ shear	∥ shear	∥ shear	⊥ shear	⊥ shear	⊥ shear	variable	variable	∥ shear	∥ shear	∥ shear	∥ shear	∥ shear	∥ shear
Banding	none	none	none	none	none	vesicle bands	vesicle bands	vesicle bands	none	none	none	vesicle bands	shear bands	shear bands	shear bands	shear bands
Spherulite area %	<1	3	14	30	60	60	20	15	50	5	<1	<1	0	3	5	15
Density (g/cm^3)	2.17	2.07	2.09	2.06	2.08	1.31	1.57	1.52	1.45	1.31	1.32	1.01	1.62	1.57	1.65	1.79
Connected vesicularity	0.08	0.10	0.16	0.11	0.16	0.25	0.27	0.21	-	0.44	0.41	0.49	0.29	0.38	0.30	0.24
TVC (wt.%)	0.33	0.27	0.39	0.33	0.39	0.45	0.40	0.42	0.29	1.22	1.17	0.80	0.74	1.30	0.77	0.55
H_2O_t (wt.%)	0.13	0.12	-	-	-	-	0.17	0.19	-	0.08	-	0.25	-	0.08	0.09	0.10

Classification data for RR samples. All data is taken from hand sample measurements except TVC (TGA) and H_2O_t (FTIR), detailed in section 3.4. ϕ_{dens} = vesicularity, d_{mode} = modal vesicle diameter, d_{mean} = mean vesicle diameter, ‘flat’ = flattened, ‘irreg’ = irregular, ∥ = parallel to, ⊥ = perpendicular to.

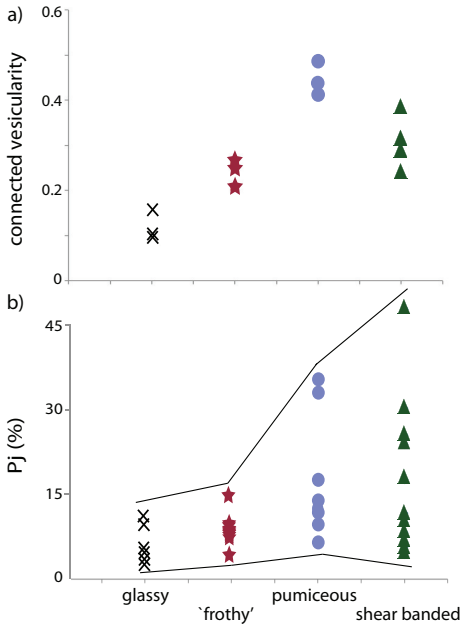

Figure 7: a) Connected vesicularity of RR lavas analysed by helium pycnometry and b) P_j of all samples measured for AMS, with lines marking upper and lower P_j limits. Symbols represent the respective sample types.

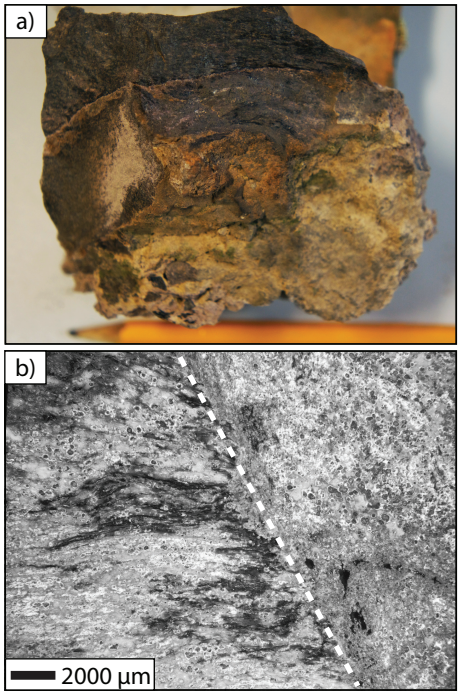

Figure 8: a) Photograph of breccia sample 47 consisting of broken clasts in a fine-grained matrix. b) Optical microscope image of breccia sample 47 showing a foliation of very high aspect ratio vesicles truncated by a healed fault (dashed white line).

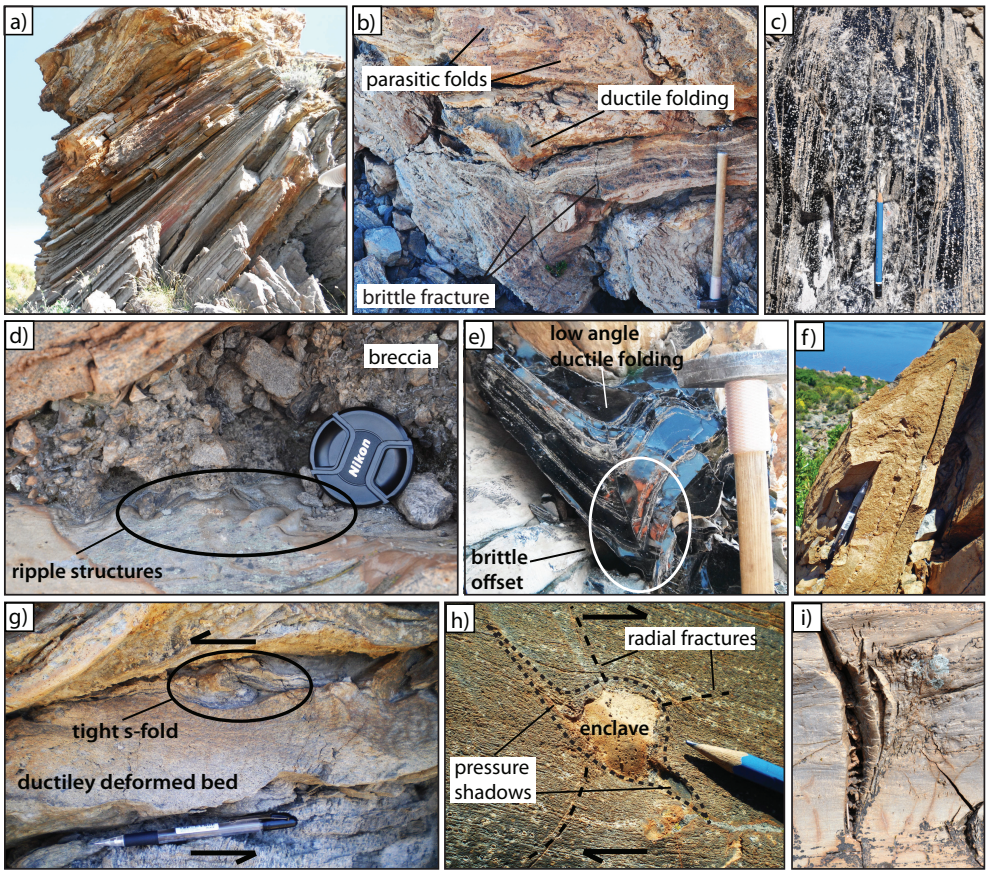

Figure 9: Photographs of various macro-textures of RR lava. a) Platy flow bands cm thick. b) Brittle faulting and ductile folding in deformed beds, hammer ∼ 60 cm long. c) Spherulite-defined banding in black obsidian lava. d) Brecciated lava between two folded bands and ductile wave-like folds, lens cap for scale, arrows give inferred sense of shear. e) Isoclinal fold in glassy obsidian bands showing fracturing and offset of spherulite trails. f) Isoclinal folding of platy layers. g) Multi-scale ductile folding. h) Rotated enclave with pressure shadows and radial fractures, indicating dextral shear i) large and small brittle tension gashes, pencil ∼ 8 cm long.

by vesicularity, spherulite content, or structurally imposed platy flow layers (Figure 9a). The latter are composed of mm to cm thick bands, delimited by detachment planes often containing breccia (Figure 9d), and are commonly highly folded and/or fractured. Spherulite bands are composed of trails of spherulitic material, often only mm thick and oriented parallel to the foliation Figure 9c).

Ductile deformation textures include many different scales and degrees of folding e.g. isoclinal folding of platy obsidian layers (Figure 9f), micro-folding superimposed on larger-scale folds (Figure 9g) and wave-like structures of thin ∼ mm wide folded bands (Figure 9d). Mixed brittle-ductile behaviour is also observed where fold hinges or folded beds are faulted and bedding is offset (Figure 9b and e), and where rotated enclaves exhibit radial fracturing (Figure 9h). Tension gashes and variably re-welded breccia infill between bands are common examples of brittle deformation found in the *RR* (Figure 9d and i). Glassy obsidian bands are sometimes observed offsetting folds, suggesting they were once the location of faults.

Section 3.1 describes significant textural heterogeneity in the *RR*. Figure 10a shows that lava

types do not vary systematically with position in the flow. All four major lava types, which correlate to vesicularity, are found both near the vent and towards the flow front, as well as on both sides of the lava flow (Figure 10a and c). Variations in the degree of shearing, vesicularity and melt viscosity also reveal high spatial diversity on a flow-wide scale. The east lobe shows higher degrees of shearing (Figure 10b), up to P_j = 48 %. This may reflect that samples were collected here almost exclusively along the lobe ridge, which is highly folded and includes many squeeze-out structures (Figure 11). These form when viscous lava extrudes through the cooling upper crust [e.g. 22].

Melt viscosity, calculated using the model of [86], with lava compositions from [35] and total dissolved water contents H_2O_t from this study, using an assumed eruptive temperature of 850 °C [37, 38] varies from $10^{8.2}$ - $10^{9.0}$ Pa s, reflecting low variability in water contents (Figure 10d). As the flow cooled during emplacement these viscosities would have increased significantly.

Figure 12 also shows how flow properties vary heterogeneously along the longitudinal, transverse and vertical transects shown in Figure 1. Since sampling was only performed on the flow surface the vertical transects show variation over the uppermost few metres of the exposed lava flow. The flow surface tends to consist of the least dense lava, as would be expected and is observed in many obsidian flows by [24] and [25]. No progression in lava type from vent to flow front are observed along longitudinal transects. Bulk susceptibility and degree of shearing vary greatly and non-systematically with position in the flow. In the 53 and 54 vertical transects P_j varies somewhat linearly but with opposite trends, showing an increase towards the flow surface in 54 but an increase with depth in 53.

3.3. Magnetic fabric

Measurements of bulk susceptibility at different temperatures for three samples (63B, glassy obsidian; 44C, 'frothy' obsidian; 39, pumiceous) shows a sharp change in slope at $\sim$ 590°C (supplementary material), marking a Curie temperature indicative of pure magnetite, Fe_3O_4. This is the only notable change with temperature, suggesting that magnetite is the dominant contributing mineral phase to AMS measurements [87, 66]. Analysis of thin sections in reflected light reveals that magnetite grains are typically elongate, with average aspect ratios of 1.8 - 2.1.

Magnetite occurs predominantly in trains aligned along deformed vesicle rims and to a lesser degree as part of spherulites or as isolated grains within the glass matrix (Figure 13). This observation, along with the crystal shape, suggests that the degree of anisotropy in each sample $P\,j$ does reflect orientations of magnetite alignments i.e. k_1 = train elongation axis. Magnetite may have crystallised preferentially on vesicle rims because they provide a suitable nucleation surface, or it could have formed after emplacement during alteration or oxidation of the lava. Regardless of magnetite origin, grain alignments replicate the trace of sheared vesicles. Therefore the intensity of the magnetic anisotropy, P_j, reflects the degree of applied shear strain.

Bulk susceptibilities range from 1.32 $\times 10^{-4}$ to 2.39 $\times 10^{-3}$ in all samples (Figure 14). As

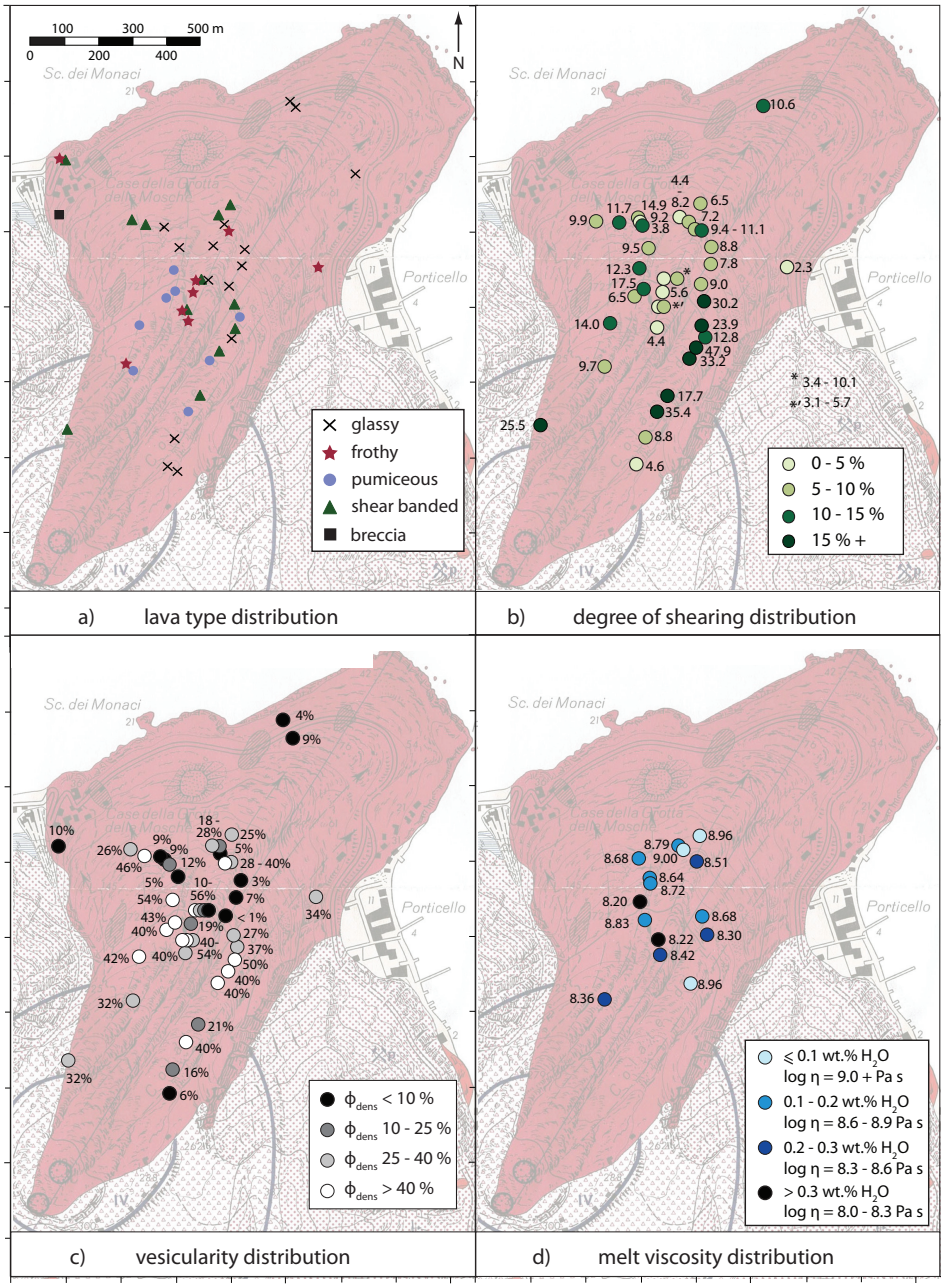

Figure 10: Maps of the Rocche Rosse flow showing a) lava type distribution, b) degree of anisotropy P_j distribution, c) vesicularity [ϕ_{dens}] and d) melt viscosity [log η] distribution, calculated using the model of [86]. Axis show latitude and longitude coordinates. Transect locations are labelled in Figure 1.

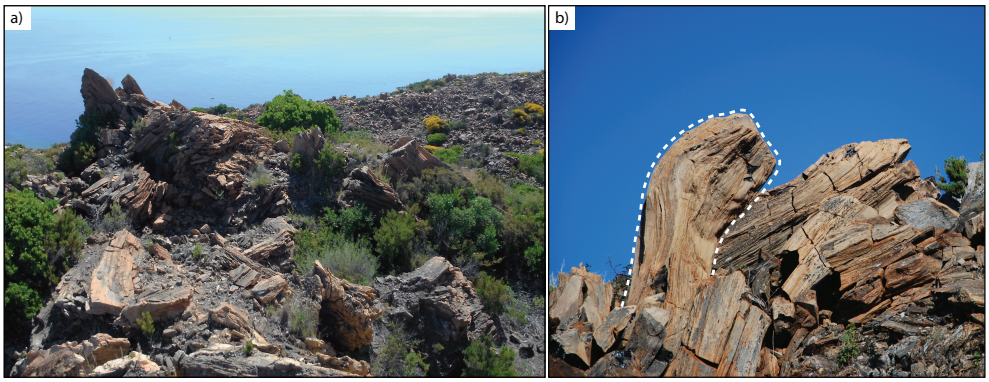

Figure 11: Photographs of a) west lobe of the RR showing strongly deformed flow surface and platy flow layers and b) a squeeze-out structure, highlighted by dashed white line.

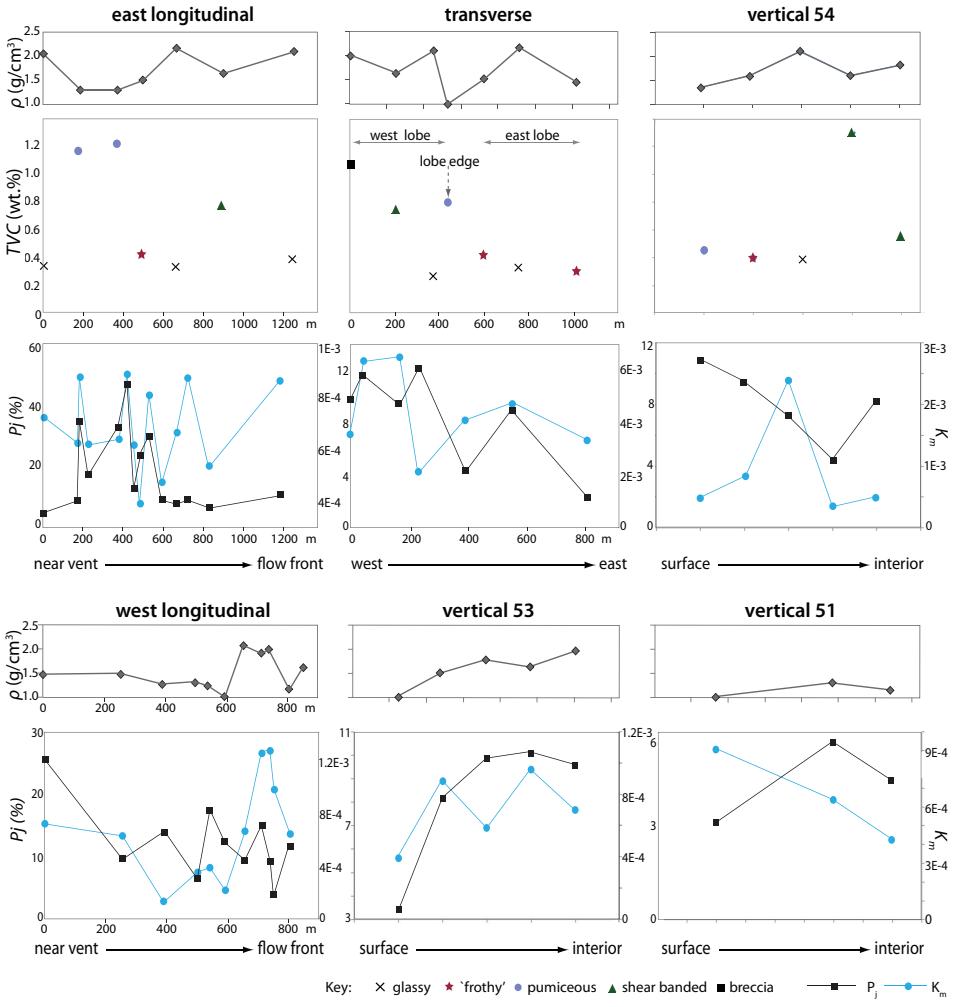

Figure 12: Longitudinal, transverse and vertical transects of several properties of the RR lava flow. Transects show variation in bulk density ρ, total volatile content TVC (data only obtained for east longitudinal, transverse and vertical 54 transects), bulk susceptibility K_m and degree of anisotropy P_j. All error bars are smaller than the size of the symbols. Transect locations are shown in Figure 1. X-axis scale for vertical transects is not known but samples were taken at approximately equal intervals over vertical heights of 3-5 metres.

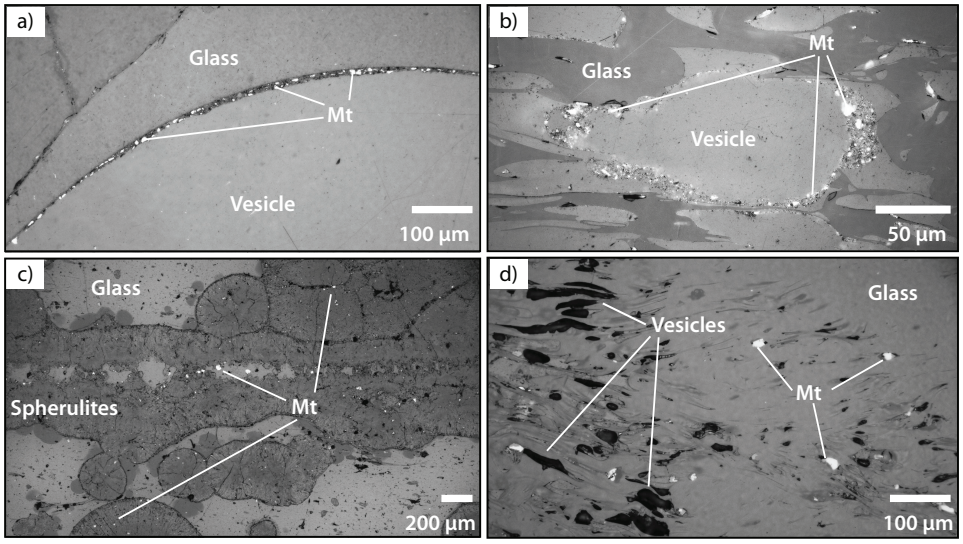

Figure 13: Reflected light images of RR thin sections showing magnetite distributions a. and b. clustered on vesicle rims, c. within spherulite trails and d. sparse magnetite grains in the glass matrix.

magnetite is the dominant contributor to AMS, K_m values are directly proportional to the amount of magnetite in each sample, confirmed by thin section analysis in reflected light (Figure 14a). There is no strong relationship between K_m and vesicularity and large variation in K_m for glassy obsidian samples (Figure 14b). This appears counterintuitive to the observation that magnetite grows preferentially on vesicle rims. However magnetite is also observed in the matrix glass (Figure 13), whose volume decreases as vesicularity increases, for a fixed sample size. An increase in vesicularity therefore results in more volume occupied by gas bubbles as opposed to magnetite-bearing glass, which offsets the increase in bubble rim surface area.

Regardless, variations in K_m across flow transects cannot be explained by variations in vesicularity (Figure 12, section 3.2). Therefore susceptibility data implies heterogeneous magnetite distributions across the flow. The three samples with the highest K_m ($> 1 \times 10^{-3}$, Figure 14b) are strongly banded obsidians containing the most numerous and well-defined spherulite bands, however aside from these three samples, K_m does not correlate with spherulite content.

3.3.1. Degree of magnetic anisotropy P_j

Samples show variable degrees of anisotropy, from 2.3 % to 47.9 % (Figure 7). P_j values $> 5\%$ are found only in rock with clear macroscopic fabric [88], for example the majority of *RR* lavas (Figures 3- 6 and 7). Previous work described P_j values as high as 4.2% - 9.5% in obsidian dome lavas [60], yet these are significantly lower than the most anisotropic *RR* samples. Pumiceous and shear banded lavas show higher P_j values (< 48 %) than glassy and 'frothy' obsidians (< 15 %, Figure 7), although low P_j values are recorded in each lava type.

3.3.2. Shape parameter T

Most samples (33 of 42) show oblate AMS ellipsoids ($k_1 \simeq k_2$) indicating a foliation, and a few show prolate fabrics ($k_1 > k_2$ and k_3), typifying a lineation (Figure 15). The foliation is predominantly oriented sub-horizontal i.e. k_3=sub-vertical (Figure 14c), indicating foliations

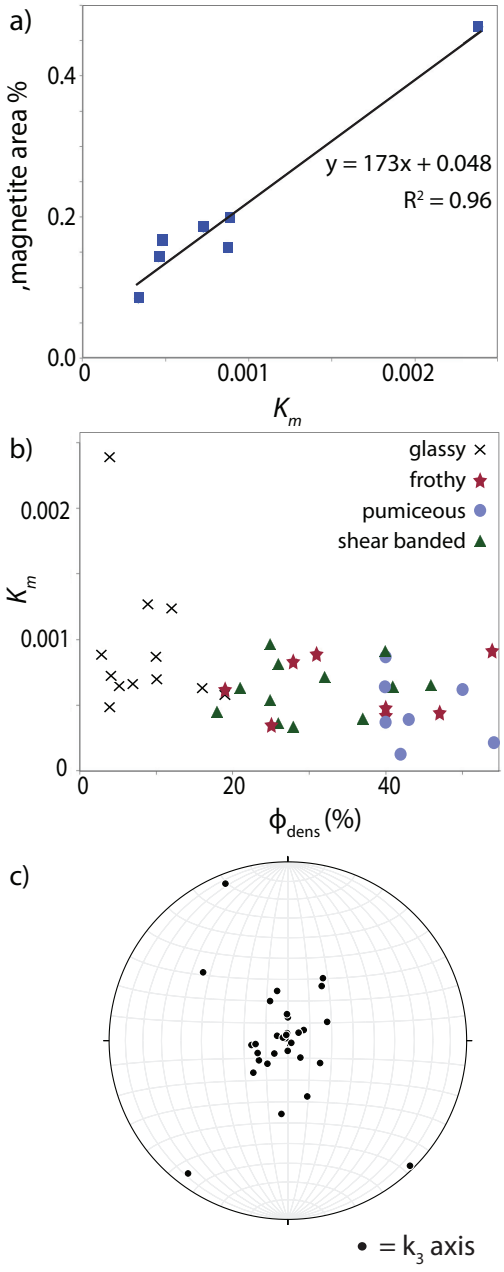

Figure 14: a) Amount of magnetite (% of thin section area), calculated from optical microscope images of thin sections, against bulk susceptibility K_m. Solid line shows best linear fit of data. b) Bulk susceptibility K_m against vesicularity for each lava type. c) Stereographic projection of all samples with oblate AMS ellipsoids, showing a predominantly sub-vertical k_3 orientation, indicating foliations parallel to the shear plane.

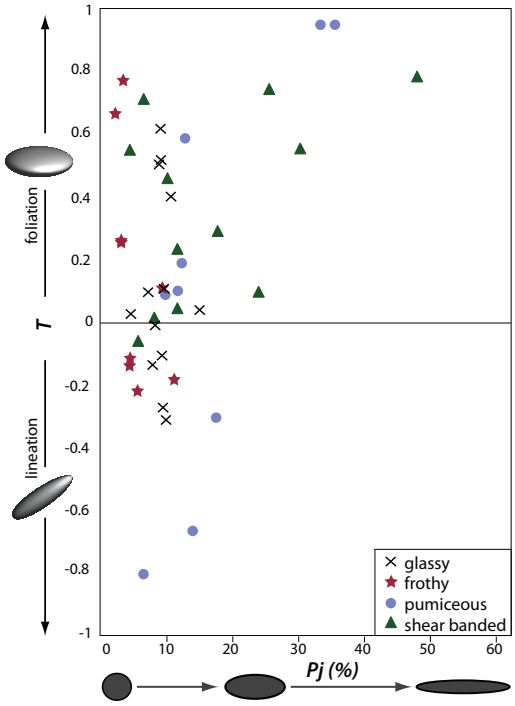

Figure 15: Plot of AMS shape parameter T against degree of anisotropy P_j. $T > 0$ = oblate fabrics $T < 0$ = prolate fabrics. Increasing P_j indicates increasing shear strain.

approximately parallel to the shear plane. The distribution of oblate and prolate fabrics with respect to degree of anisotropy is shown in Figure 15. The most sheared samples tend to record a foliation, however there is a notable range in fabric shape within the same lava type. Note again how the shear banded lava samples record some of the highest P_j values.

3.4. Water content variability

Total volatile contents TVC derived from TGA measurements range from 0.27 wt.% to 1.30 wt.%. Analysis of degassing rate with temperature indicates that several volatile phases contribute to the bulk TVC value (Table 2). The patterns of volatile release on heating provide insights into the relative contributions of primary and secondary water in the glasses [89, 72, 83, 73]. In most samples the predominant dTG peak and mass loss is in the 250-550 °C temperature range, which is thought to correspond to strongly bound molecular water present in pore spaces, usually ascribed to meteoric water [89]. It can also represent adsorbed meteoric water in samples containing < 1 wt.% TVC [73]. Contributions from weakly-bound H_2O_m (< 250 °C) and halogens (> 1000 °C) are much less significant.

The amount of volatile loss in the temperature range associated with magmatic water ($\sim$ 550-1000 °C, [89, 73]) shows a very weak correlation with TVC. Bulk volatile results are therefore assumed to predominantly reflect the amount of meteoric (or secondary water) in *RR* samples i.e. hydration post-emplacement. Lava types group in two distinct areas on a plot of peak degassing temperature against TVC (Figure 16, see also supplementary material). Glassy obsidian (type 1) and 'frothy' obsidian (type 2) have the lowest TVC and the highest peak degassing temperature, whereas pumiceous (type 3) and shear banded (type 4) samples have higher TVC and consistently low peak degassing temperatures (see also [81]). Although

Table 2: TGA volatile analysis results

Sample	Type	TVC (wt.%)	Peak temp (°C)	< 250°C (wt.%)	250-550°C (wt.%)	550-1000°C (wt.%)	> 1000°C (wt.%)
35	glassy	0.266	991	0.041	0.096	0.048	0.080
44C	glassy	0.291	1032	0.041	0.100	0.117	0.034
62	glassy	0.329	1049	0.046	0.053	0.152	0.078
3	glassy	0.335	1125	0.074	0.093	0.086	0.079
48	glassy	0.385	790	-0.043	0.065	0.216	0.061
54B2	glassy	0.386	n/a	0.087	0.108	0.080	0.112
54A3	'frothy'	0.399	1153	0.055	0.139	0.066	0.136
50	'frothy'	0.420	275	0.057	0.103	0.124	0.136
54A2	'frothy'	0.451	1026	0.094	0.165	0.115	0.076
54C2	shear banded	0.552	318	-0.014	0.268	0.165	0.131
18	shear banded	0.745	298	0.120	0.345	0.171	0.111
55	shear banded	0.766	343	0.056	0.415	0.183	0.113
36	pumiceous	0.800	303	0.015	0.324	0.309	0.148
16	pumiceous	1.169	275	0.201	0.640	0.246	0.083
57	pumiceous	1.217	302	0.131	0.726	0.192	0.163
54C1	shear banded	1.298	350	0.173	0.675	0.314	0.135

Results from thermogravimetric analysis. TVC is total volatile content, peak temp is peak degassing temperature and the last four columns show sample weight loss measured in each temperature range.

texture additionally influences the temperature of volatile loss, with vesicular samples degassing at lower temperatures due to shorter diffusive path lengths [73], we can nonetheless broadly group the major lava types into those that have experienced significant (types 3 and 4) and insignificant hydration (types 1 and 2).

Lava types form distinct groupings on a plot of TVC against total vesicularity (Figure 17a). Glassy obsidians cluster in the low TVC, low vesicularity corner and 'frothy' obsidians, despite their high vesicle content, are equally poorly-hydrated. Both pumiceous samples and shear banded lavas have higher TVC and shear banded lavas are notable in that they plot on a continuum between the lowest and highest hydrated water content i.e. between pumiceous and glassy obsidians. Hydration does not correlate well with total vesicularity (Figure 17a), however, it does correlate well with connected vesicularity (Figure 17b). Within shear banded lavas there is a marked decrease in connected vesicularity as TVC and vesicularity decrease (Figure 17a), which is accompanied by a general increase in the degree of shearing P_j.

FTIR analysis reveals a range in H_2O_t between 0.08 wt.% and 0.25 wt.% (Figure 18a), with standard deviations of $\pm$0.01 wt.% to $\pm$0.08 wt.%. Carbon dioxide peaks were below detection. These water contents are significantly lower than those measured for the bulk samples by TGA (Table 1). Lava samples show a much greater dispersion than in Figure 17 and vary across the full range of measured H_2O_t. It is notable that some pumiceous and sheared samples have lower H_2O_t than vesicle-free obsidians, and that sheared samples can be significantly more water-rich than relatively unsheared pumiceous samples. An H_2O_m:H_2O_t speciation plot (Figure 18b) suggests that samples contain relatively insignificant amounts of molecular water dissolved in the glass.

Transects of H_2O_t and H_2O_m variations in banded obsidian and 'frothy' samples show localised H_2O_t heterogeneities within samples as well as between them. All three samples measured (50, 41 and 54A3) are composed of adjacent bands or lenses of obsidian glass

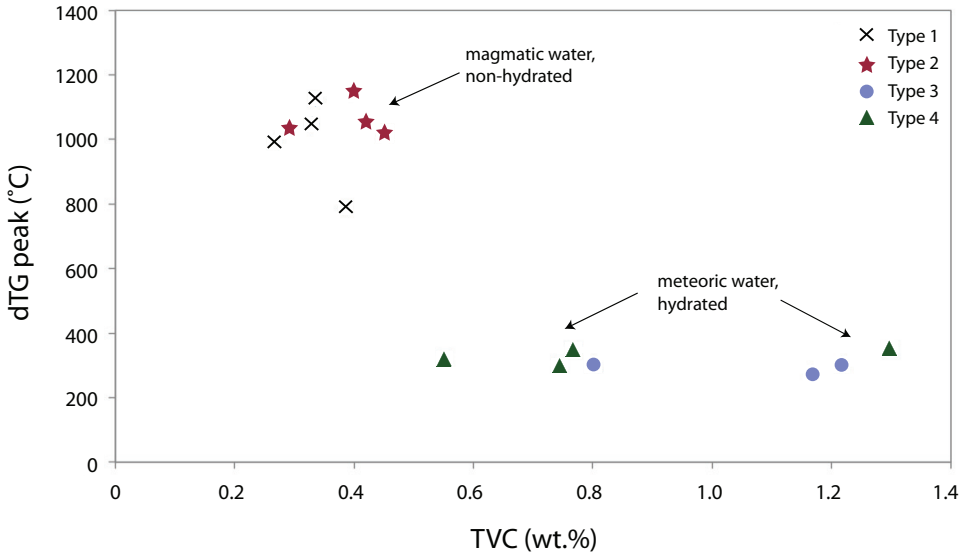

Figure 16: Peak degassing temperature of RR samples against total volatile content TVC. Symbols show RR lava types, described in Section 3.1.

and 'frothy' material. Accurate measurements could not be performed on sample 54A3 due to high spherulite content. Results show that H_2O_t increases approximately linearly in both other samples towards and into the 'frothy' band and away from the glass (Figure 18c). H_2O_m variability is low and does not change linearly between lava types, suggesting that water diffusion predominantly involves OH^-.

4. Discussion

4.1. Analysis of AMS method

The high degree of strain localisation observed are thought to be responsible for the variable degrees of shearing P_j recorded in the *RR*. Localised heterogeneities common to shear zones and lava flows [e.g. 90, 28, 91] could have been overlooked depending on the size of the sample measured, resulting in a bulk measurement that does not reflect local variations in the sample [56, 63]. This can explain the spread of P_j down to low values, which is recorded across all lava types (Figure 7). For example, samples 55 and 54C1 both have low P_j despite showing highly sheared vesicle textures (Figure 6c and f). However they also both display strongly localised deformation textures (Figure 6d and j). Therefore the value of P_j will be high only if high strain was homogeneously applied to a region of approximately the same size of the measured sample. Therefore whilst AMS analysis offers a rapid and simple alternative to x-ray tomography for quantifying deformation fabrics we conclude that AMS results can only be correctly interpreted when combined with a detailed petrographic study. Low degrees of shearing may also arise from complex shearing or multiple shearing episodes, as seen in the experiments of [92].

4.2. Discrimination between magmatic and meteoric water

The assumption made here that bulk volatile contents TVC largely reflect post emplacement rehydration of the lava by meteoric water is based upon the proposal that peak degassing

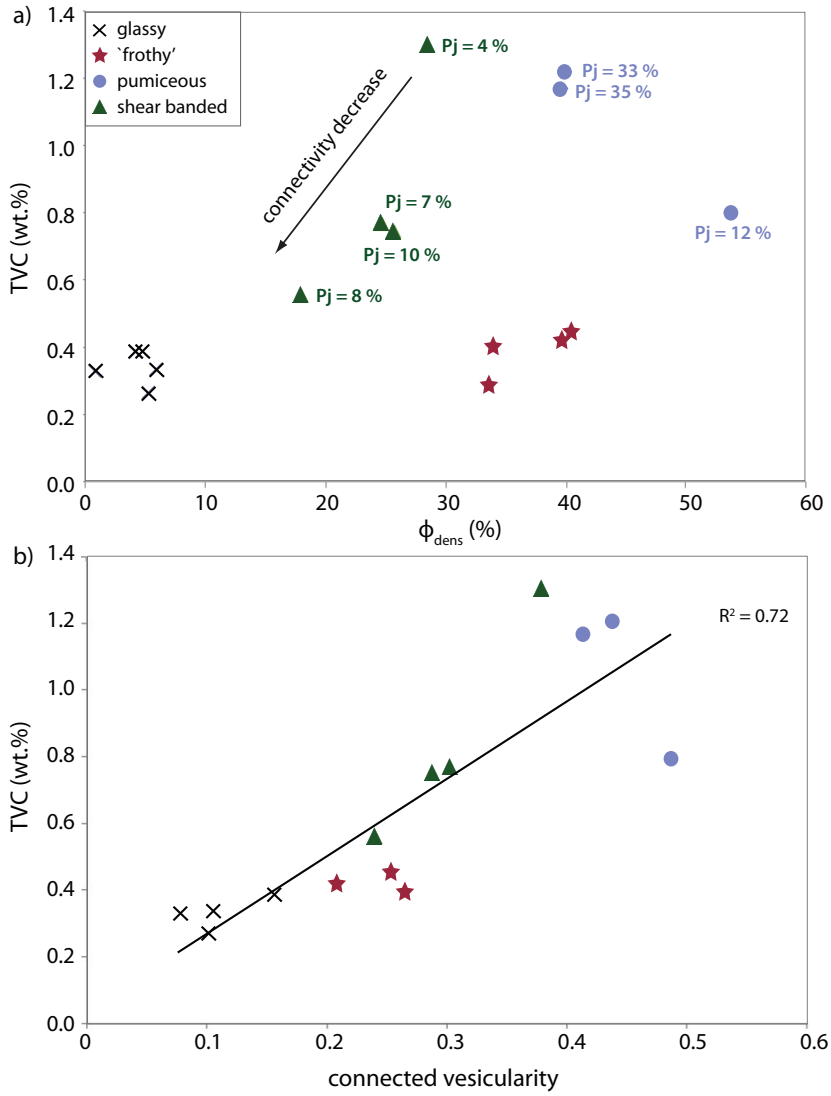

Figure 17: a) Total volatile content TVC [wt.%] against total vesicularity [%] and b) TVC [wt.%] against connected vesicularity. P_j values for pumiceous and shear banded samples are indicated. Arrow shows decrease in connected vesicularity of shear banded samples with decreasing vesicularity, also shown in b).

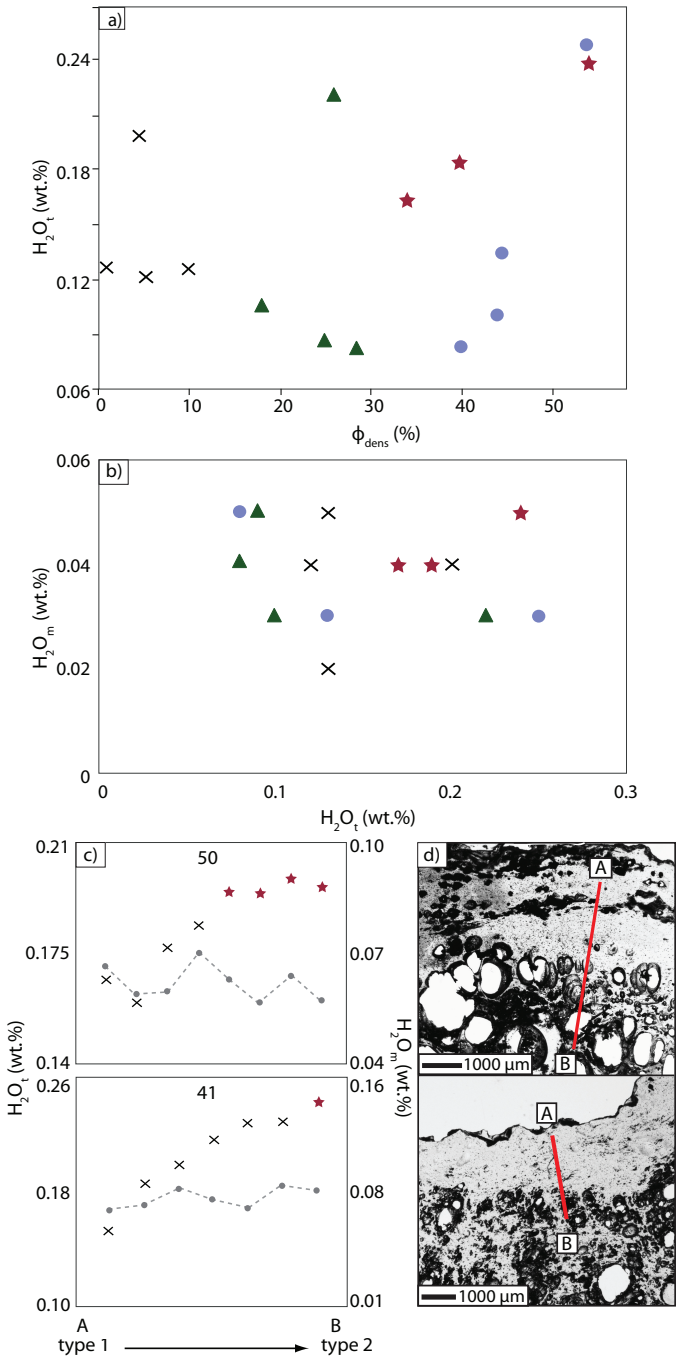

Figure 18: a) H_2O_t in wt.% against vesicularity [ϕ_{dens} in %]. Symbols are the same as in Figure 17. b) H_2O_m against H_2O_t data, measured by FTIR, showing predominantly low molecular water. c) Line maps of H_2O_t across glassy (crosses) and 'frothy' (stars) bands showing an enrichment towards higher vesicularity bands. Variation in H_2O_m across the transects is also shown (grey symbols). d) Transect locations shown in optical microscope images of FTIR wafers. Measurements were made at approximately equal intervals along the transects.

temperatures reflect water speciation [e.g. 89, 72, 83]. A previous study by [73], however, found that experimental volcanic glass lost magmatic water in the temperature range 250-550 °C, ordinarily associated with meteoric water. Nonetheless, these samples contain over 4 wt.% total water, and samples with higher volatile concentrations are known to degas at lower temperatures [81]. For samples with water contents similar to those in this study, all measured peak degassing temperatures were over 550 °C [73].

The difference between water contents measured by TGA and by FTIR is therefore thought to be due to the TGA method sampling the bulk rock, including vesicle walls, whereas FTIR only measures water contents in the glass, away from vesicles. Glass surrounding vesicles is the most likely location for rehydration, because meteoric water percolates into the lava through vesicles and cracks. Furthermore, vesicle walls may contain additional water as a result of bubble resorption during lava cooling, a process whereby an increase in water solubility with decreasing temperature [93] results in diffusion of molecular water back into the melt prior to solidification [80]. Spatial heterogeneities in water observed in the samples (Figure 18c) may therefore either reflect different extents of degassing at atmospheric pressures, or variable volatile resorption during cooling. However, the latter case would be expected to create high H_2O_m:H_2O_t ratios, which are not seen in the glasses (Figure 18b). Furthermore, Figure 18c reveals that water diffusion between bands generally involves OH^- and not molecular water, and is therefore not related to low temperature resorption or rehydration.

4.3. Effect of shear on obsidian degassing and outgassing

The macro- and micro-scale textures observed in the *RR*, as well as the degree of shear-induced magnetic anisotropy, provide a record of the internal shearing experienced during flow of an effusive silicic lava. Shear deformation of the exsolved gas phase (bubbles) can be tracked through textures showing bubble elongation and coalescence and high connected vesicularity (e.g. Figure 5 and Figure 7), development of permeability through connected gas planes, localisation of strain into narrow bands of high shear (e.g. Figure 6), volatile loss, reduction in connected vesicles and densification of the magma through welding of vesicles to produce glassy obsidian bands (e.g. Figure 3 and Figure 7). We propose that this textural record explains the evolution from pumiceous lava (type 3) through shear banded lava (type 4) to outgassed, glassy obsidian (type 1).

We also see evidence for outgassing via shear-induced fracture and healing of the melt, also observed during shearing of analogue silicic magma samples [94, 17] and in natural samples [e.g. 8, 12, 11, 13]. Figure 19 shows a field example of the fracture-healing process in full, whereby stage 1 is represented by vesiculation of a water-rich band, potentially from being brought to the surface in a squeeze out structure during emplacement. The stage 2 band shows brittle fracture of a weak, bubble-rich plane, when viscous shear of unrelaxed (high viscosity, high local strain-rate) magma leads to local accumulation of shear stress, sufficient to induce brittle deformation and fracture the magma [95]. If connectivity to lower pressures is achieved, the sudden stress release and pressure drop on fracture development induces rapid outgassing of both the volatiles inside the bubbles and the melt immediately surrounding the fracture, similar to the process shown by the work of [10] and explored in more detail by [11]. Gas loss instigates welding of magma fragments to form a bubble-free, dense, higher

viscosity, 'healed' obsidian band (stage 3 in Figure 19).

The breccia we observe in the *RR* (Figure 8) is interpreted here as part of the "sub planar breccia zone" described by [13] outcropping in the NW of the flow, and it results from welding of large fractured lava clasts. Variably re-welded breccia layers between obsidian bands (Figure 9d and i) provide evidence for local crossings of the glass transition into the brittle domain and subsequent healing of fractured material. Indeed, textures revealing fracture, healing and subsequent viscous deformation are recognised throughout the entire Monte Pilato-Rocche Rosse explosive-effusive eruptive sequence [13]. The flow banding pervading the lava flow is also attributed to continual brittle-ductile reworking of heterogeneous magma [6, 12, 14, 16].

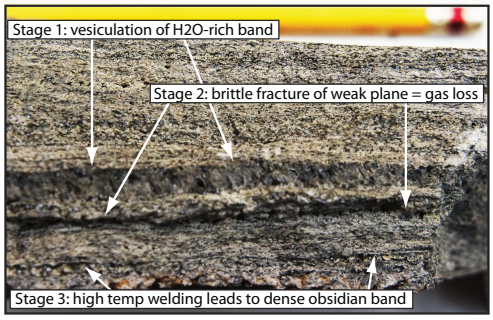

Figure 19: Photograph of sample with ∼ 5 mm wide 'frothy' layer and many ∼ mm wide obsidian bands, showing different stages (explained in text) of the fracture-healing process. Pencil for scale.

Spherulitic material is often found in trails along obsidian bands (e.g. Figure 19) corroborating the notion proposed by [44, 96] and [97] that spherulites preferentially nucleate and grow in flow bands of high strain. Expulsion of water upon growth of spherulites leads to local enrichment in melt volatile content [45] by up to 0.2 wt.% [98] as well as increased diffusion and mobility of volatiles in the melt [44]. Spherulite growth may also be responsible for significant heating, to above initial eruption temperatures [22]. These effects of spherulite formation could significantly reduce melt viscosity and possibly induce secondary vesiculation of the melt [99]. Spherulite formation may therefore assist in continuation of the shear fracturing process by maintaining melt in the brittle-ductile deformation field.

4.3.1. Post eruptive hydration

The effect of shear on sample hydration post eruption can be observed by combining textural, volatile and magnetic data. Figure 17b illustrates that high connected vesicularity i.e. increased bubble coalescence leads to increased secondary hydration. Furthermore bubble connectivity increases with continued deformation [100, 101], leading to outgassing. This, in turn, leads to a drop in bubble connectivity and decreased secondary hydration because rain water can no longer easily circulate through the obsidian. Further shearing-induced vesicularity loss results in almost bubble-free obsidians, where connected vesicularity and hence hydration are low. These results provide additional insights to previous studies showing a correlation between vesicle content and hydration [102], and indicate that vesicle connectivity has a greater control on secondary water content than simply vesicularity [73].

The 'frothy' obsidians observed throughout the *RR* are not significantly hydrated despite vesicularities of 30-60%. This is a result of their low aspect ratio vesicles, showing little coalescence parallel to the shear direction (Figure 4e), resulting in low connected vesicularities (Figure 7). 'Frothy' lavas show plentiful evidence for originating from glassy obsidians via secondary exsolution of volatiles during flow emplacement [23]. The vesicles are relatively unsheared but still describe bubble expansion in an extensional regime perpendicular to shear (Figure 4f). 'Frothy' bands are often found in fold hinges, suggesting that bubbles nucleate as a result of a drop in pressure in the extensional environment of the hinge. This lava type is similar to the large gas cavities described by [103] and attributed to creation of void space upon buckling of the cooling flow surface, which is likely to be another mechanism for generation of 'frothy' obsidian.

4.4. Model for obsidian formation

Glass volatile concentrations suggest that vesicular lava falls into two groups according to their water content (Figure 20). Upon shearing, lava in the higher H_2O_t group would lose vesicularity and water i.e. outgas and form dense obsidian lava. Densification would occur through either collapse of a connected bubble network [e.g. 104] or healing of fractures [e.g. 12]. Lower H_2O_t vesicular samples have on average 0.13 wt.% dissolved water, compared to approximately 0.19 wt.% in the obsidian samples. Using a simple model based on the ideal gas law [similar to that used in 105] we calculate that a 0.06 wt.% decrease in dissolved water content can be explained by exsolution of bubbles corresponding to the observed porosity increase of 35% ('vesiculation' arrow in Figure 20). We therefore propose that this lower H_2O_t group could form by re-vesiculation of obsidian at *RR* eruption temperatures (850 °C, [37, 38]) and pressures equivalent to approximately 100 m magma depth (2 MPa), the estimated flow thickness of the *RR* [32]. For vesiculation at pressures equal to the flow surface, a more likely scenario considering the prevalence of less dense magma nearer the surface (Figure 12), closed-system degassing of obsidian cannot explain observed low water contents in vesicular samples. This would indicate that either 1) the magma experienced non-equilibrium closed-system degassing, related to its high viscosity [2] or 2) a proportion of the gas was also being removed from the vesiculating magma (open-system degassing, [105]). High bubble connectivity in vesicular samples supports this theory (Figure 7). Alternatively, vesicular samples may have been zones of localised heating during deformation, reducing water solubility [93].

These findings suggest a cyclical nature to the outgassing history of obsidian. Overall variation in water content is small (< 0.2 wt.%), reflecting the fact that changes in porosity are occurring at low pressures and represent the final stages in obsidian formation. The last stage in the vesiculation-outgassing-densification cycle prior to lava solidification is what ultimately determines final lava porosity. For example, 'frothy' lava represents recent volatile exsolution in a low pressure environment that cooled before the bubbles could be sheared by further flow advance. In the following two paragraphs we discuss evidence that numerous outgassing cycles are also required during ascent in the conduit in order to generate obsidian lava.

Data from melt inclusions in the obsidian suggest initial H_2O contents of 2.5 wt.% for the

latitic melt trigger and 3.5 wt.% for the rhyolitic end member [38], which erupted first explosively as the Monte Pilato sequence and then effusively $\sim$ 400 years later as the *RR* lava flow. Considering that explosive and effusive products are of similar composition, we assume an approximately equal water content for both types of product, prior to their ascent in the conduit. Therefore approximately 3.4 wt.% water loss occurred prior to eruption. Previous work has recognised both shear fracturing and development of permeable bubble networks as important gas loss mechanisms occurring during magma ascent [e.g. 8, 15, 106, 13].

If we consider volatile removal via shear-induced fracture alone, the maximum water loss as a result of a single fracture, as measured by [13], is only 0.14 wt.% in both explosive and effusive products from the Monte Pilato-Rocche Rosse eruption. Detailed degassing studies on tuffisite-bearing obsidian from Chaitén showed slightly higher water loss between 0.2 and 0.3 wt.% towards tuffisite vein margins [11]. And shear experiments on silicic magma analogues by [17] showed that, in samples with multiple fractures, magmatic water decreased by 0.8 to 1.4 wt.% during deformation. This last water loss estimate is high, because experimental samples underwent rapid fracture healing due to high confining pressures and a lack of pore fluid pressure, which greatly enhances repeated fracture formation and hence water loss [94], whereas fractures in natural obsidian would take much longer to heal [107].

Regardless, these levels of outgassing would be insufficient to result in the 3.4 wt.% water loss necessary for observed *RR* water contents of $\sim$ 0.08-0.25 wt.%, as well as those measured in many other obsidians [108, 109, 110, 45, 13]. Therefore, in order to account for gas removal of an entire magma body by shear fracturing, there would have to be multiple cycles of fracturing and healing occurring throughout magma ascent [15, 13]. The theory of continuous, cyclical outgassing is further supported by seismic evidence from other volcanoes, whereby earthquake repose times match calculated obsidian fracture healing times [12, 10, 107]. Outgassing is also likely to occur via collapse of bubble networks, however [100, 9, 106], which may be the dominant mechanism at greater depths in the conduit i.e. several thousand metres [9]. Therefore its likely that water loss and compaction of vesicular magma through shear-induced bubble deformation, in addition to repeated fracture and healing, prevented explosive fragmentation and led to the generation of dense obsidian lava.

Figure 21 shows the proposed model for generation of the *RR* lava, based on the textural, magnetic and geochemical evidence described in this paper. Coloured rectangles show the textural types we observe in the *RR*, similar to the textural stages we infer also represent the stages of outgassing during ascent in the conduit. Rounded rectangles, with the exception of surface vesiculation of glassy obsidian to 'frothy' obsidian, represent the different processes that may occur in the cyclical evolution from a water-rich rhyolite source magma to water-poor obsidian lava. As a silica-rich magma decompresses it vesiculates as pressure decreases ('pumiceous' lava). High shear strains ($\uparrow \gamma$) lead to deformation of bubbles ($\uparrow AR$), a vesicularity decrease ($\downarrow \phi_{dens}$) and volatile loss ($\downarrow H_2O$) once a permeable network is established ('shear banded lava'). Further shear-induced outgassing results in a more vesicle-poor, volatile poor magma ('obsidian'). Further decompression leads to further volatile exsolution and repetition of the process. Multiple outgassing cycles in the conduit, a requirement of which may be slow magma ascent rates [7, 16], lead to the eventual development of the

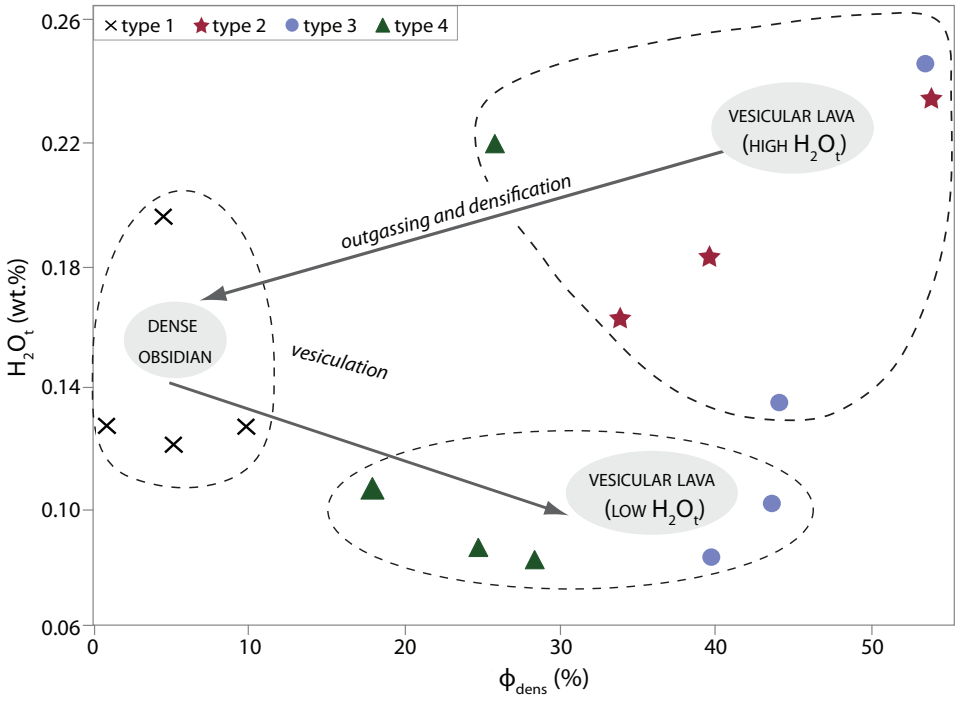

Figure 20: Magmatic water content [wt.%] of RR samples against vesicularity [%], showing inferred outgassing and vesiculation paths between lava samples.

outgassed silicic lava we observe on the surface.

4.5. Role of heterogeneities on structural evolution of an obsidian flow

The *RR* flow surface displays complexity and structural heterogeneity on multiple scales. There is no longitudinal progression from more vesicular lava near the vent to obsidian at the flow front and sides, which would support the theory of gradual collapse of pumiceous lava during emplacement [5] and proposed by [32] for the *RR*. Rather shear deformation processes occurring down to microscopic scales during weeks of surface flow [35] overprint any flow-scale morphology. The dominant effect of surface deformation on observed textures may be a symptom of the high-alkali calc-alkaline composition and high eruptive temperature, which produce a less viscous and more mobile obsidian lava, prolonging viscous flow [38, 39, 40]. Using the model of [86], *RR* composition data from [35] and an eruptive temperature of 850 °C [37, 38], a melt viscosity on the order of 10^8 - 10^9 Pa s is calculated for the *RR*. This is at the low end of the range of measured magma viscosities of other effusive silicic eruptions [e.g. 111, 112, 1]. Ubiquitous strain localisation and related squeeze-out structures have also been linked to the exceptional mobility of highly viscous lava flows [22, 1].

Results indicate that emplacement is driven in part by gravity, as foliation data suggests pure shear dominates throughout the flow, in agreement with other lava flow studies [90, 26], but the structural evolution of the flow is largely controlled by localised deformation as a result of heterogeneities within the lava. Flow banding occurs on a range of scales. Ramp structures composed of platy obsidian layers with brecciated material in between comprise the largest-scale flow banding observed in the *RR*. They are testament to extreme textural heterogeneity

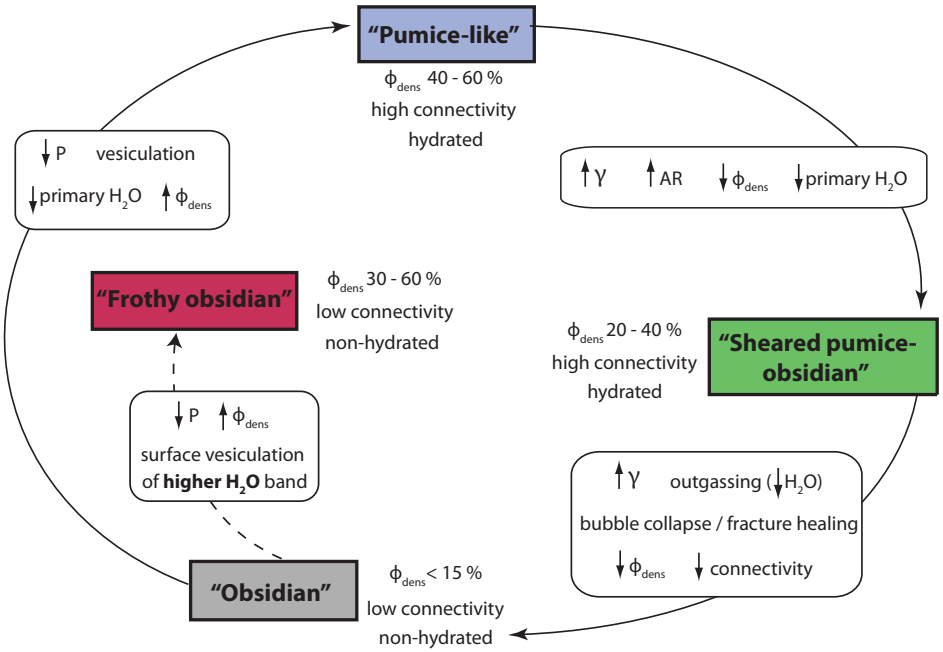

Figure 21: Model for generation of RR lavas, with lava types representing the final stages of the shearing cycle before complete cooling. ϕ_{dens} is vesicularity, γ is shear strain, AR is vesicle aspect ratio and P is pressure.

where brittle behaviour is localised between dense obsidian bands. Micron to millimetre-wide bands may be defined by microlites or vesicularity, the former thought to reflect varying degrees of undercooling [110] and the latter attributed to heterogeneous water contents.

Figure 18b shows extremely localised differences in water concentration in bands of adjacent glassy obsidian and 'frothy' obsidian (0.04 - 0.10 wt.%). The approximately linear increase towards the vesicular material suggests that 'frothy' bands are enriched in volatiles relative to the glass and are therefore zones for preferential late-stage exsolution upon surface folding [see also 97]. The degassed band is less likely to vesiculate as it has already lost water through the outgassing mechanisms previously described. Adjacent bands therefore display discrete degassing histories reflecting previously higher water content bands where the vesiculation-outgassing-densification cycle took place, resulting in a lower water content. Vesiculation is later favoured in the adjacent, now relatively higher water content band. Such sensitivity to water content may be key to formation of repeated vesicle-rich, vesicle-poor obsidian bands. Small variations in texture can also lead to strain localising preferentially due to rheological (viscosity) contrasts between layers. This is observed in the macro-folding of alternating pumiceous and obsidian bands [16], described by [113] in several rhyolitic obsidian flows, who observe a correlation between thickness ratios of vesicular to non-vesicular bands and the type of folding that develops.

The importance of strain localisation on the distribution of water in obsidian is shown by both magmatic and meteoric water analyses. Local increases in melt H_2O can result from shear-induced bubble collapse and resorption [114, 115], and growth of spherulites [116, 98]. The opposite, a localised melt H_2O decrease, may occur with bubble exsolution and out-

gassing via bubble networks or fractures [10, 11], both of which may conversely lead to a local increase in meteoric water content [e.g. 102, 98].

5. Conclusions

Using a combination of geochemical, textural, permeability and magnetic analyses we characterise the extreme heterogeneity often observed in obsidian flows and attempt to unravel the wide range of deformation processes preserved in lava textures in the Rocche Rosse flow, Lipari. Four major textural lava types are identified based on vesicle content, shape and connected vesicularity and linked to flow structures on micron to metre scales. Measurements of magmatic and meteoric water content are combined with 2D and 3D textural observations to show that:

a) shear-induced connected vesicularity exerts a primary control on lava hydration post-eruption. This builds upon previous work proposing that hydration is a function of vesicle surface area per unit volume of glass.

b) the range of measured magmatic water contents is low (0.08 - 0.25 wt.%) and reflects significant outgassing and low pressure degassing which creates high textural variability in the lava flow. Water content transects between adjacent vesicular and glassy obsidian bands reveal highly localised differences in dissolved volatiles, which lead to preferential exsolution of high water bands at the expense of previously outgassed low water bands, suggesting an effective feedback mechanism for obsidian band formation. The importance of spherulite growth on the continued formation of flow bands is also discussed.

We present evidence that dense obsidian lava forms from vesicular lava by progressive shearing and outgassing via bubble networks and fractures and densification through bubble collapse and fracture healing. Conversely we show how vesicular lava can then result from decompression-induced vesiculation of obsidian. We describe a model for obsidian generation which requires multiple iterations of the vesiculation-outgassing-densification cycle during magma ascent in order to result in an effusive, as opposed to explosive, eruption of silicic lava. Surface lavas preserve the final stage of this cycle prior to cooling in an exceptional textural heterogeneity, which overprints flow-scale morphology and governs the mobility, emplacement and structural evolution of the Rocche Rosse flow.

6. Acknowledgements

This research was supported by NERC grant (NE/J500033/1). Additionally the authors are grateful to the following: Charles Clapham and Donovan Hawley for assistance with sample coring (Engineering Workshop, University of Bristol), Richard Brooker for technical support during FTIR sample preparation and analysis (Experimental Petrology Research Laboratory, University of Bristol), and to Eva Hartung and David Floess for performing magnetic susceptibility and anisotropy measurements (Section of Earth and Environmental Sciences, University of Geneva). We are grateful to Thomas Shea and an anonymous reviewer for their comments which greatly improved the manuscript.

7. Appendix

7.1. Supplementary material

7.1.1. Calibration of DSC-TGA measurement

Figure 22 shows the TGA curve of the Al_2Ol_3 standard used to calibrate the TGA measurement. It illustrates the weight change that is recorded when sample weight remains constant throughout heating. Variability in the reading is assumed to be due to a buoyancy correction in the instrument, whereby a hotter, more expanded sample is expected to weigh less. Figure 22 also illustrates the close fit between the second heating curve performed on the first sample measured, and the standard heating curve, indicating that all volatiles are lost during the first heating cycle.

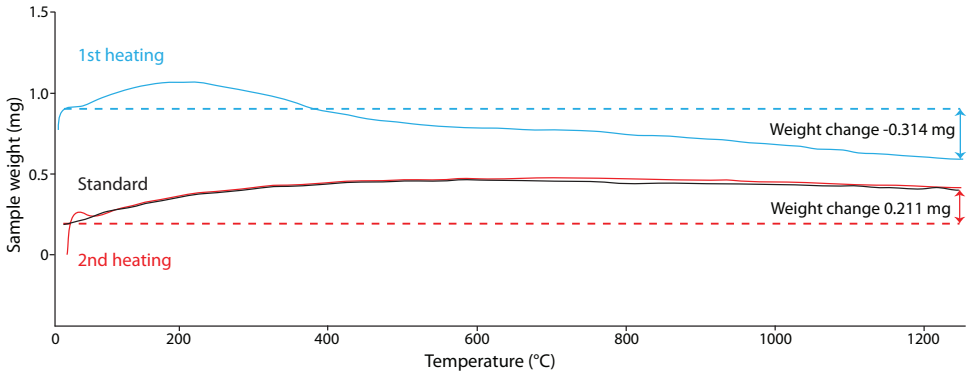

Figure 22: TGA curves of Al_2O_3 standard (black curve) and sample 57 showing weight change recorded during first heating (green curve) and second heating cycles (blue curve).

7.1.2. Example dTG curves

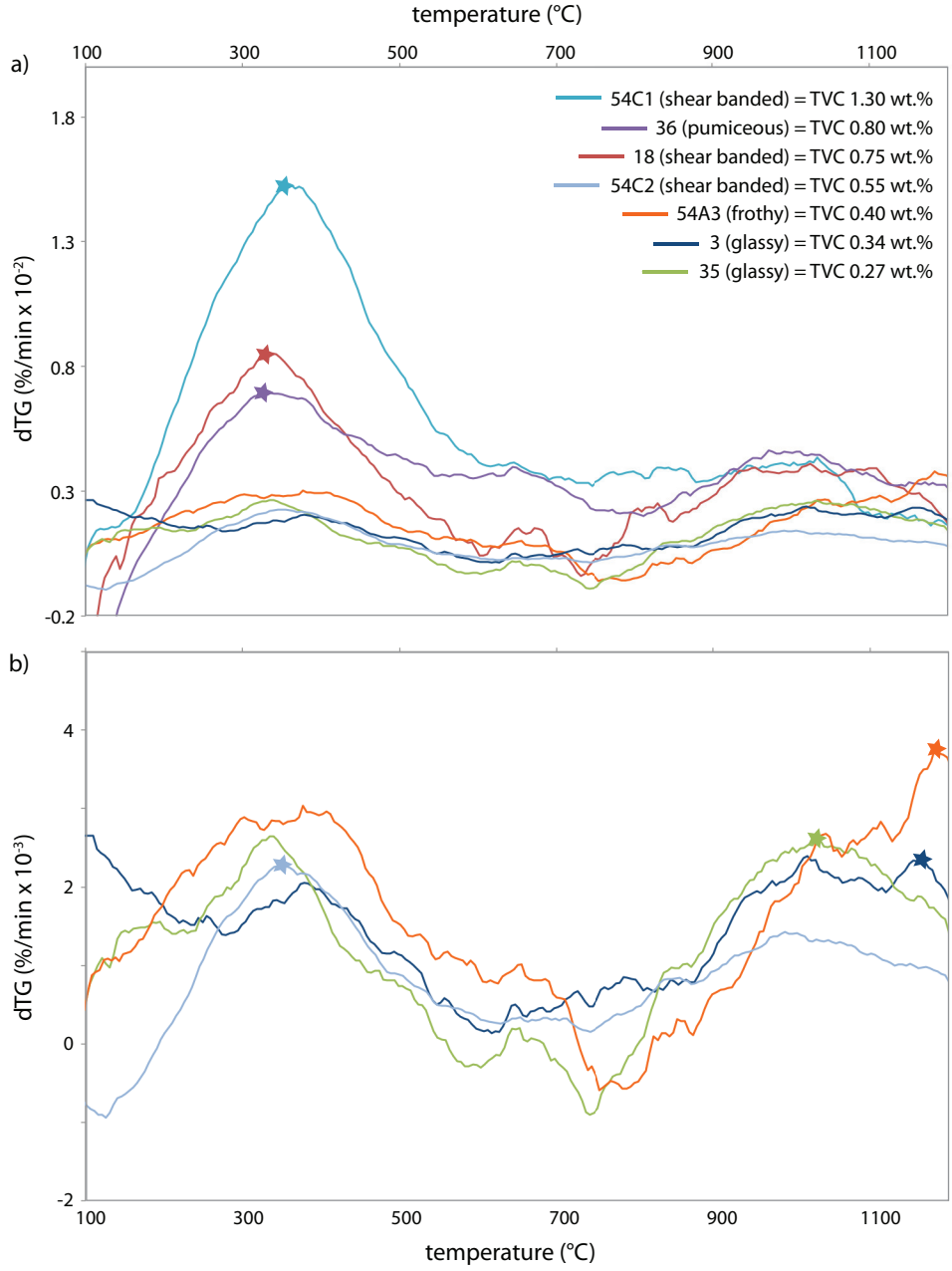

Figure 23: a) Rate of weight loss with time (dTG) against temperature for several RR samples analysed by TGA. Total volatile content (TVC) of each sample shown in legend. b) Subset of samples shown in a), vertical scale enlarged. Stars indicate peak degassing temperature, also shown in Figure 16.

7.1.3. Identification of contributory magnetic minerals

Temperature analysis gives a Curie temperature of 590 ° C during both the heating and the cooling cycles, indicating pure magnetite Fe_3O_4. However, the maximum susceptibility values reached upon cooling are much higher than the maximum reached during the heating cycle (Figure 24). Several authors have also observed this and attribute it to the creation of new magnetite during heating [117, 61]. Temperature analysis is also carried out down to temperatures of below -196 °C, the point at which the Verwey phase transition occurs

in magnetite [118] i.e. the temperature at which the mineral records an abrupt decrease in conductivity [119]. This transition is not seen however in the three samples unless they had been heated previously (to observe the Curie temperature). This indicates alteration of magnetite and therefore the observation of 'new' magnetite created upon heating is most likely simply due to slight recrystallization of altered phases during the cooling stage of the high temperature measurement (personal correspondence: Agico).

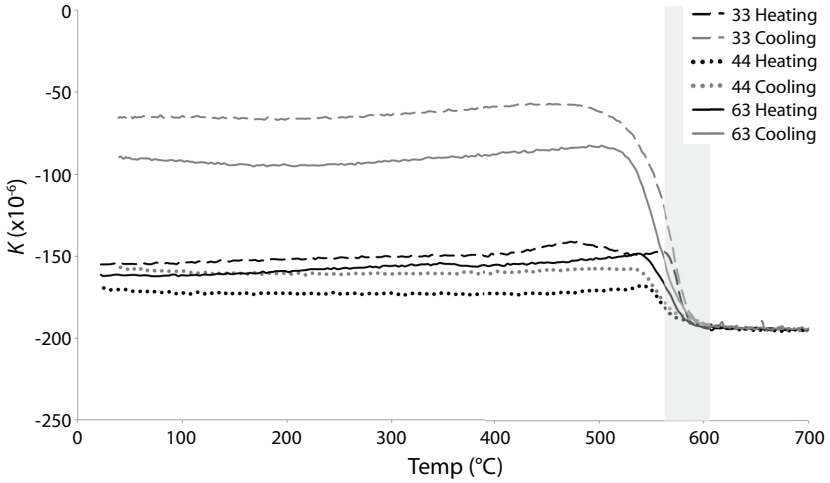

Figure 24: Thermomagnetic heating and cooling curves of three RR samples, showing susceptibility K against temperature °C. grey rectangle shows Curie temperature region.

[1] J. Farquharson, M. R. James, H. Tuffen, Examining rhyolite lava flow dynamics through photo-based 3D reconstructions of the 20112012 lava flowfield at Cordn-Caulle, Chile, Journal of Volcanology and Geothermal Research 304 (2015) 336–348.

[2] R. Sparks, The dynamics of bubble formation and growth in magmas: a review and analysis., Journal of Volcanology and Geothermal Research 3 (1978) 1–37.

[3] H. Gonnermann, Magma fragmentation, Annual Review of Earth and Planetary Sciences 43 (2015) 431–458.

[4] B. Taylor, J. Eichelberger, H. Westrich, Hydrogen isotope evidence of rhyolitic magma degassing during shallow intrusion and eruption, Nature 306 (1983) 541–545.

[5] J. Eichelberger, C. Carrigan, H. Westrich, R. H. Price, Non-explosive silicic volcanism, Nature 323 (1986) 598–602.

[6] H. Gonnerman, M. Manga, Explosive volcanism may not be an inevitable consequence of magma fragmentation., Nature 426 (2003) 432–435.

[7] C. Jaupart, C. Allegre, Gas content, eruption rate and instabilities of eruption regime in silicic volcanoes, Earth and Planetary Science Letters 102 (1991) 413–429.

[8] M. V. Stasiuk, J. Barclay, M. R. Carroll, C. Jaupart, J. C. Ratte, R. S. J. Sparks, S. R. Tait, Degassing during magma ascent in the Mule Creek vent (USA), Bulletin of Volcanology 58 (1996) 117–130.

[9] S. Okumura, M. Nakamura, S. Takeuchi, A. Tsuchiyama, T. Nakano, K. Uesugi, Magma deformation may induce non-explosive volcanism via degassing through bubble networks, Earth and Planetary Science Letters 281 (2009) 267–274.

[10] A. Cabrera, R. Weinberg, H. Wright, Melt fracturing and healing: A mechanism for degassing and origin of silicic obsidian, Geology 39 (2010) 67–70.

[11] J. Castro, B. Cordonnier, H. Tuffen, M. J. Tobin, L. Puskar, M. C. Martin, H. A. Bechtel, The role of melt-fracture degassing in defusing explosive rhyolite eruptions at volcan Chaiten, Earth and Planetary Science Letters 333-334 (2012) 63–69.

[12] H. Tuffen, D. Dingwell, H. Pinkerton, Repeated fracture and healing of silicic magma generate flow banding and earthquakes?, Geology 31 (2003) 1089.

[13] A. Cabrera, R. Weinberg, H. Wright, Magma fracturing and degassing associated with obsidian formation: the explosive-effusive transition, Journal of Volcanology and Geothermal Research.

[14] J. M. Castro, D. B. Dingwell, A. R. L. Nichols, J. E. Gardner, New insights on the origin of flow bands in obsidian, Geological Society of America Special Papers 396 (2005) 55–65.

[15] H. Tuffen, D. B. Dingwell, Fault textures in volcanic conduits: evidence for seismic trigger mechanisms during silicic eruptions, Bulletin of Volcanology 67 (2005) 370–387.

[16] H. M. Gonnerman, M. Manga, Flow banding in obsidian: A record of evolving textural heterogeneity during magma deformation, Earth and Planetary Science Letters 236 (2005) 135–147.

[17] J. K. Shields, H. M. Mader, M. Pistone, L. Caricchi, D. Floess, B. Putlitz, Strain-induced outgassing of three-phase magmas during simple shear, Journal of Geophysical Research 119 (2014) 6936–6957.

[18] S. Okumura, M. Nakamura, K. Uesugi, T. Nakano, T. Fujioka, Coupled effect of magma degassing and rheology on silicic volcanism, Earth and Planetary Science Letters 362 (2013) 163–170.

[19] K. Sano, K. Wada, E. Sato, Rates of water exsolution and magma ascent inferred from microstructures and chemical analyses of the Tokachi-Ishizawa obsidian lava, Shirataka, northern Hokkaido, Japan, Journal of Volcanology and Geothermal Research 292 (2015) 29–40.

[20] J. M. Castro, I. N. Bindeman, H. Tuffen, I. C. Schipper, Explosive origin of silicic lava: Textural and H2O evidence for pyroclastic degassing during rhyolite effusion, Earth and Planetary Science Letters 405 (2014) 52–61.

[21] C. Schipper, J. Castro, H. Tuffen, M. R. James, P. How, Shallow vent architecture during hybrid explosiveeffusive activity at Cordn Caulle (Chile, 201112): Evidence from direct observations and pyroclast textures, Journal of Volcanology and Geothermal Research 262 (2013) 25–37.

[22] H. Tuffen, B. Cordonnier, J. M. Castro, Modelling the thermal effects of spherulite growth in rhyolitic lava. Abstract V11C-2782, Presented at 2012 Fall Meeting, AGU, San Francisco (2012) 3–7 Dec.

[23] J. H. Fink, S. W. Anderson, C. R. Manley, Beyond the Permeable Foam Model, Journal of GeophysicalResearch 97 (1992) 9073–9083.

[24] J. Fink, Structure and emplacement of a rhyolitic obsidian flow: Little Glass Mountain, Medicine Lake Highland, northern California, Geological Society Of America Bulletin 94 (1983) 362–380.

[25] C. Manley, J. Fink, Internal textures of rhyolite flows as revealed by research drilling Internal textures of rhyolite flows as revealed by research drilling, Geology 15 (1987) 549–552.

[26] J. Castro, M. Manga, K. Cashamn, Dynamics of obsidian flows inferred from microstructures : insights from microlite preferred orientations, Earth and Planetary Science Letters 199 (2002) 211–226.

[27] A. C. Rust, M. Manga, K. V. Cashman, Determining flow type , shear rate and shear stress in magmas from bubble shapes and orientations, Journal of Volcanology and Geothermal Research 122 (2003) 111–132.

[28] G. Ventura, The strain path and kinematics of lava domes: An example from Lipari (Aeolian Islands, Southern Tyrrhenian Sea, Italy), Journal of Geophysical Research 109 (2004) 1–10.

[29] E. Cañón Tapia, Factors affecting the relative importance of shape and distribution anisotropy in rocks: theory and experiments., Tectonophysics 340 (2001) 117–131.

[30] H. Pichler, Carta Geologica dell Isola di Lipari, scale 1:10,000, Instituto di Vulcanologia, CNR.

[31] J. C. Tanguy, M. Le Goff, C. Principe, S. Arrighi, V. Chillemi, A. Paliotti, S. La Delfa, G. Patane, Archeomagnetic dating of Mediterranean volcanics of the last 2100 years: validity and limits, Earth and Planetary Science Letters 211 (2003) 111–124.

[32] M. Davì, R. Rosa, F. Holtz, Mafic enclaves in the rhyolitic products of Lipari historical eruptions ; relationships with the coeval Vulcano magmas (Aeolian Islands , Italy), Bulletin of Volcanology 72 (2010) 991–1008.

[33] H. Pichler, The Island of Lipari., Rendiconti Societa Italiana di Minerologia e Petrologia. 36 (1980) 415–440.

[34] A. Gioncada, R. Mazzuoli, M. Bisson, M. Pareschi, Petrology of volcanic products younger than 42 ka on the Lipari-Vulcano complex (Aeolian Islands, Italy); an example of volcanism controlled by tectonics, Journal of Volcanology and Geothermal Research 122 (2003) 191–220.

[35] J. Gottsman, D. Dingwell, The cooling of frontal flow ramps: a calorimetric study on the Rocche Rosse rhyolite flow, Lipari, Aeolian Islands, Italy, Terra Nova 13 (2001) 157–164.

[36] G. Lanzo, S. Basile, M. Brai, S. Rizzo, Volcanic products of Lipari (Aeolian Islands, Italy): Multivariate analysis of petrographic and radioetric data., Radiation Measurements 45 (2010) 816–822.

[37] R. F. A. Cas, J. Wright, Volcanic successions: modern and ancient, Unwin Hyman, London.

[38] M. Davì, The Rocche Rosse rhyolitic lava flow (Lipari, Aeolian Islands): magmatological and volcanological aspects, EJM European Journal of Mineralogy 33 (2007) 1–8.

[39] M. Davì, R. De Rosa, P. Donato, R. Sulpizio, The Lami pyroclastic succession (Lipari, Aeolian Islands): A clue for unravelling the eruptive dynamics of the Monte Pilato rhyolitic pumice cone, Journal of Volcanology and Geothermal Research 210 (2011) 285–300.

[40] F. Forni, F. Lucchi, A. Peccerillo, C. A. Tranne, P. L. Rossi, M. L. Frezzotti, Stratigraphy and geological evolution of the Lipari volcanic complex (central Aeolian archipelago), In: The Aeolian Islands Volcanoes. Geological Society, London, Memoirs (2013) 213–279.

[41] H. Davì, M.and Behrens, R. Vetere, F.and De Rosa, The viscosity of latitic melts from Lipari (Aeolian Islands, Italy): Inference on mixingmingling processes in magmas, Chemical Geology 259 (2009) 89–97.

[42] G. A. J. Cole, G. W. Butler, On the lithophyses in the obsidian of the Rocche Rosse, Lipari., Quaterly Journal of the Geological Society 48 (1892) 438–443.

[43] D. Gimeno, Devitrification of natural rhyolitic obsidian glasses: petrographic and microstructural study (SEM+EDS) of recent (Lipari island) and ancient (Sarrabus, SE Sardinia) samples, Journal of Non-Crystalline Solids 323 (2003) 84–90.

[44] P. Clay, B. O'Driscoll, R. Gertisser, H. Busemann, S. C. Sherlock, S. P. Kelley, Textural characterization, major and volatile element quantification and ArAr systematics of spherulites in the Rocche Rosse obsidian flow, Lipari, Aeolian Islands: a temperature continuum growth model, Contributions to Mineralogy and Petrology 165 (2012) 373–395.

[45] J. Castro, P. Beck, H. Tuffen, A. Nichols, D. Dingwell, M. C. Martin, Timescales of spherulite crystallization in obsidian inferred from water concentration profiles, American Mineralogist 93 (2008) 1816–1822.

[46] F. Von Aulock, B. Kennedy, C. Schipper, J. Castro, D. Martin, C. Oze James, P. Watkins, M. amd Wallace, L. Puskar, F. Begue, A. Nichols, H. Tuffen, Advances in Fourier transform infrared spectroscopy of natural glasses: From sample preparation to data analysis, Lithos 206-209 (2014) 52–64.

[47] J. Watkins, M. Manga, C. Huber, M. Martin, Diffusion-controlled spherulite growth in obsidian inferred from H2O concentration profiles, Contributions to Mineralogy and Petroogy 157 (2009) 163–172.

[48] H. Gonnerman, M. Manga, The Fluid Mechanics Inside a Volcano, Annual Review of Fluid Mechanics 39 (2007) 321–356.

[49] Y. Bottinga, D. F. Weill, Densities of liquid silicate systems calculated from partial molar volumes of oxide components., American Journal of Science 269 (1970) 169–182.

[50] R. A. Lange, I. S. A. Carmichael, Densities of Na20-K20-Ca0-Mg0-Fe0-Fe203-A1203-Ti02-Si02 liquids: New measurements and derived partial molar properties, Geochimica et Cosmochimica Acta 51 (1987) 2931–2946.

[51] R. A. Ketcham, Three-dimensional grain fabric measurements using high-resolution x-ray computed tomography., Journal of Structural Geology 27 (2005) 1217–1228.

[52] D. Tarling, F. Hrouda, The Magnetic Anisotropy of Rocks., Chapman and Hall, 1993.

[53] E. Cañón Tapia, G. Walker, E. Herrero-Bervera, The internal structure of lavas: insights from AMS measurements II: Hawaiian pahoehoe, toothpaste lava and aa, Journal of Volcanology and Geothermal Research 76 (1997) 19–46.

[54] S. Loock, H. Diot, B. Van Wyk de Vries, P. Launeau, O. Merle, F. Vadeboin, M. Petronis, Lava flow internal structure found from AMS and textural data: An example in methodology from the Chane des Puys, France, Journal of Volcanology and Geothermal Research 177 (2008) 1092–1104.

[55] E. Ferré, A. Gébelin, J. L. Till, C. Sassier, K. Burmeister, Deformation and magnetic fabrics in ductile shear zones: A review, Tectonophysics 629 (2014) 179–188.

[56] G. Borradaile, Magnetic susceptibility, petrofabrics and strain., Tectonophysics 156 (1988) 1–20.

[57] G. Borradaile, Correlation of strain with anisotropy of Magnetic susceptibility (AMS)., Pure Applied Geophysics 135 (1991) 15–29.

[58] P. Rochette, M. Jackson, C. Aubourg, Rock magnetism and the interpretation of anisotropy of magnetic susceptibility., Reviews of Geophysics 30 (1992) 209–226.

[59] E. Cañón Tapia, Anisotropy of magnetic susceptibility of lava flows and dykes: a historical account, Magnetic Fabric: Methods and Applications Geological Society (1994) 205–225.

[60] E. Cañón Tapia, J. Castro, AMS measurements on obsidian from the Inyo Domes, CA: a comparison of magnetic and mineral preferred orientation fabrics., Journal of Volcanology and Geothermal Research 134 (2004) 169–182.

[61] B. Almqvist, S. Bosshard, A. Hirt, H. B. Mattsson, G. Hetenyi, Internal flow structures in columnar jointed basalt from Hrepphlar, Iceland: II. Magnetic anisotropy and rock magnetic properties, Bulletin of Volcanology 74 (2012) 1667–1681.

[62] B. Housen, B. A. van der Pluijm, E. J. Essene, Plastic behavior of magnetite and high strains obtained from magnetic fabrics in the Parry Sound shear zone, Ontario Grenville Province, Journal of Structural Geology 17 (1995) 265–278.

[63] M. A. Evans, M. T. Lewchuk, R. D. Elmore, Strain partitioning of deformation mechanisms in limestones: examining the relationship of strain and anisotropy of magnetic susceptibility (AMS) , Journal of Structural Geology 25 (2003) 1525–1549.

[64] F. Hrouda, M. Chlupacova, K. Schulmann, P. md, J.and Zvada, On the effect of lava viscosity on the magnetic fabric intensity in alkaline volcanic rocks, Stud. Geophys. Geod. 49 (2005) 191–212.

[65] V. Jelinek, Characterization of the magnetic fabric of rocks., Tectonophysics 79 (1981) T63–T67.

[66] D. Gubbins, E. Herrero-Bervera, Encyclopedia of Geomagnetism and Paleomagnetism., Springer, 2007.

[67] Y. Formenti, T. Druitt, Vesicle connectivity in pyroclasts and implications for the fluidisation of fountain-collapse pyroclastic flows, Montserrat (West Indies), Earth and Planetary Science Letters 214 (2003) 561–574.

[68] W. Degruyter, O. Bachmann, A. Burgisser, Controls on magma permeability in the volcanic conduit during the climactic phase of the Kos Plateau Tuff eruption (Aegean Arc), Bulletin of Volcanology 72 (2010) 63–74.

[69] J. Blundy, K. Cashman, Petrologic reconstruction of magmatic system variables and processes, Reviews in Mineralogy and Chemistry 69 (2008) 179–239.

[70] S. Newman, E. Stolper, S. Epstein, Measurement of water in rhyolitic glasses: calibration of an infrared spectroscopic technique., American Mineralogist 71 (1986) 1527–1541.

[71] H. Tuffen, J. Owen, J. Denton, Magma degassing during subglacial eruptions and its use to reconstruct palaeo-ice thicknesses., Earth-Science Reviews 99 (2010) 1–18.

[72] J. Denton, H. Tuffen, J. Gilbert, Variations in hydration within perlitised rhyolitic lava-sevidence from Torfajkull, Iceland, Journal of Volcanology and Geothermal Research 223-224 (2012) 64–73.

[73] T. Giachetti, H. Gonnermann, T. Gardner, J.and Shea, A. Gouldstone, Discriminating secondary from magmatic water in rhyolitic matrix-glass of volcanic pyroclasts using thermogravimetric analysis, Geochimica et Cosmochimicha Acta 148 (2015) 457–476.

[74] J. Dixon, E. Stolper, J. Holloway, An experimental study of water and carbon dioxide solubilities in mid-ocean ridge basaltic liquids. Part I: calibration and solubility models., Journal of Petrology 156 (1995) 302–314.

[75] Y. Zhang, H2O in rhyolitic glasses and melts: Measurement, speciation, solubility, and diffusion, Reviews of Geophysics 37 (1999) 493.

[76] D. B. Dingwell, S. Webb, Relaxation in silicate melts, European Journal of Mineralogy 2 (1990) 427–449.

[77] Y. Zhang, R. Belcher, P. Ihinger, L. Wang, Z. Xu, S. Newman, New calibration of infrared measurement of water in rhyolitic glasses., Geochimica et Cosmochimicha Acta 61 (1997) 3089–3100.

[78] P. Ihinger, Y. Zhang, E. Stolper, The speciation of dissolved water in rhyolitic melt, Geochimica et Cosmochimicha Acta 63 (1999) 3567–3578.

[79] Y. Zhang, Z. Xu, H. Behrens, Hydrous species geospeedometer in rhyolite: Improved calibration and application, Geochimica et Cosmochimicha Acta 64 (2000) 3347–3355.

[80] I. McIntosh, E. W. Llewellin, M. Humphreys, A. Nichols, A. Burgisser, C. I. Schipper, J. Larsen, Distribution of dissolved water in magmatic glass records growth and resorption of bubbles., Earth and Planetary Science Letters 401 (2014) 1–11.

[81] J. Denton, H. Tuffen, J. Gilbert, N. Odling, The hydration and alteration of perlite and rhyolite, Journal of the Geological Society 166 (2009) 895–904.

[82] L. Applegarth, H. Tuffen, M. James, H. Pinkerton, Degassing-driven crystallisation in basalts, Earth-Science Reviews 116 (2013) 1–16.

[83] H. Tuffen, J. Owen, L. Applegarth, Measurement of volatile concentrations in volcanic glasses using thermogravimetric analysis: comparison with micro-analytical methods, Poster presented at EGU 2012.

[84] P. Ihinger, R. Hervig, P. McMillan, Analytical Methods for Volatiles in Glasses, Volatiles in Magmas, in Reviews in Mineralogy 30 (1994) 67–122.

[85] S. Okumura, M. Nakamura, S. Nakashima, Determination of molar absorptivity of IR fundamental OH-stretching vibration in rhyolitic glasses, American Mineralogist 88 (2003) 1657–1662.

[86] D. Giordano, J. K. Russell, D. B. Dingwell, Viscosity of magmatic liquids: A model, Earth and Planetary Science Letters 271 (2008) 123–134.

[87] T. Nagata, Rock magnetism, 2nd Edition, Maruzen, 1961.

[88] R. Butler, Paleomagnetism: Magnetic domains to geologic terranes, Vol. Chapter 8, Blackwell Scientific, 1992.

[89] M. Roulia, K. Chassapis, J. a. Kapoutsis, E. I. Kamitsos, T. Savvidis, Influence of thermal treatment on the water release and the glassy structure of perlite, Journal of Materials Science 41 (2006) 5870–5881.

[90] O. Merle, Internal strain within lava flows from analogue modelling., Journal of Volcanology and Geothermal Research 81 (1998) 189–206.

[91] T. Shea, E. Hellebrand, H. Gurioli, L. ad Tuffen, Conduit- to localized-scale degassing during Plinian eruptions: Insights from major element and volatile (Cl and H2O) analyses within Vesuvius AD 79 pumice, Journal of Petrology 55 (2014) 315–344.

[92] E. Cañón Tapia, H. Pinkerton, The anisotropy of magnetic susceptibility of lava flows: an experimental approach, Journal of Volcanology and Geothermal Research 98 (2000) 219–233.

[93] A. Ryan, J. Russell, A. Nichols, K. Hess, L. Porritt, Experiments and models on H2O retrograde solubility in volcanic systems, American Mineralogist 100 (2015) 774–786.

[94] S. Okumura, M. Nakamura, T. Nakano, K. Uesugi, A. Tsuchiyama, Shear deformation experiments on vesicular rhyolite: Implications for brittle fracturing, degassing, and compaction of magmas in volcanic conduits, Journal of Geophysical Research 115 (2010) 1–10.

[95] H. Wright, R. Weinberg, Strain localization in vesicular magma: Implications for rheology and fragmentation, Geology 37 (2009) 1023–1026.

[96] S. Seaman, M. D. Dyar, N. Marinkovic, The effects of heterogeneity in magma water concentration on the development of flow banding and spherulties in rhyolitic lava., Journal of Volcanology and Geothermal Research 183 (2009) 157–169.

[97] S. J. Seaman, Microtexture development during rapid cooling in three rhyolitic lava flows, American Mineralogist 98 (2013) 304–318.

[98] F. W. Von Aulock, A. R. L. Nichols, B. M. Kennedy, C. Oze, Timescales of texture development in a cooling lava dome, Geochimica et Cosmochimica Acta 114 (2013) 72–80.

[99] A. N. McArthur, R. A. F. Cas, G. J. Orton, Distribution and significance of crystalline, perlitic and vesicular textures in the Ordovician Garth Tuff (Wales) , Bulletin of Volcanology 60 (1998) 260–285.

[100] S. Okumura, M. Nakamura, A. Tsuchiyama, T. Nakano, K. Uesugi, Evolution of bubble microstructure in sheared rhyolite: Formation of a channel-like bubble network, Journal of Geophysical Research 113 (2008) 1–18.

[101] L. Caricchi, A. Pommier, M. Pistone, J. Castro, A. Burgisser, D. Perugini, Strain-induced magma degassing: insights from simple-shear experiments on bubble bearing melts, Bulletin of Volcanology 73 (2011) 1245–1257.

[102] T. Giachetti, H. Gonnerman, Water in volcanic pyroclast: Rehydration or incomplete degassing?, Earth and Planetary Science Letters 369-370 (2013) 317–332.

[103] J. Castro, K. V. Cashman, N. Joslin, B. Olmsted, Structural origin of large gas cavities in the Big Obsidian Flow, Newberry Volcano, Journal of Volcanology and Geothermal Research 114 (2001) 313–330.

[104] H. Westrich, J. Eichelberger, Gas transport and bubble collapse in rhyolitic magma: an experimental approach, Bulletin of Volcanology 56 (1994) 447–458.

[105] J. Owen, H. Tuffen, D. W. McGarvie, Explosive subglacial rhyolitic eruptions in Iceland are fuelled by high magmatic H2O and closed-system degassing, Geology 41 (2013) 251–254.

[106] S. Okumura, M. Nakamura, T. Nakano, K. Uesugi, A. Tsuchiyama, Experimental constraints on permeable gas transport in crystalline silicic magmas, Contributions to Mineralogy and Petrology 164 (2012) 493–504.

[107] S. Yoshimura, M. Nakamura, Fracture healing in a magma: An experimental approach and implications for volcanic seismicity and degassing, Journal of Geophysical Research 115 (2010) 1–14.

[108] J. Eichelberger, H. Westrich, Magmatic volatiles in explosive rhyolitic eruptions, Geophysical Research Letters 8 (1981) 757–760.

[109] P. J. DeGroat-Nelson, B. I. Cameron, J. H. Fink, J. R. Holloway, Hydrogen isotope analysis of rehydrated silicic lavas: implications for eruption mechanisms., Earth and Planetary Science Letters 185 (2001) 331–341.

[110] J. Castro, M. Manga, M. C. Martin, Vesiculation rates of obsidian domes inferred from H2O concentration profiles, Geophysical Research Letters 32 (2005) 1–5.

[111] A. Goto, A new model for volcanic earthquake at Unzen volcano: Melt rupture model., Geophysical Research Letters 26 (1998) 2541–2544.

[112] R. S. J. Sparks, M. D. Murphy, A. M. Lejeune, R. B. Watts, J. Barclay, S. R. Young, Control on the emplacement of the andesite lava dome of the Soufriere Hills volcano, Montserrat by degassing-induced crystallization, Terra Nova 12 (2000) 14–20.

[113] J. Castro, K. V. Cashman, Constraints on rheology of obsidian lavas based on mesoscopic folds, Journal of Structural Geology 21 (1999) 807–819.

[114] T. Yoshimura, M. Nakamura, Diffusive dehydration and bubble resorption during open-system degassing of rhyolitic melts., Journal of Volcanology and Geothermal Research 178 (2008) 72–80.

[115] J. M. Watkins, M. Manga, D. J. De Paolo, Bubble geobarometry: a record of pressure changes, degassing and regassing at Mono craters, California., Geology 40 (2012) 699–702.

[116] R. S. J. Sparks, Causes and consequences of pressurization in lava dome eruptions, Earth and Planetary Science Letters 150 (1997) 177–189.

[117] F. Hrouda, A technique for the measurement of thermal changes of magnetic susceptibility of weakly magnetic rocks by the CS-2 apparatus and KLY-2 Kappabridge, Geophysics Journal International 118 (1994) 604–612.

[118] T. Nagata, K. Kobayashi, M. D. Fuller, Identification of magnetite and hematite in rocks by magnetic observations at low temperature., Journal of Geophysical Research 69 (1964) 2111–2120.

[119] Z. Zhang, S. Satpathy, Electron states, magnetism, and the Verwey transition in magnetite, Physical Review B 44 (1991) 13319–13331.